Modelling the UV and Optical Emission from Accretion Disks around Supermassive Black Holes

Alexander Scott Weston

Supervisor: Professor Ian M. McHardy

A dissertation presented for the degree of
Master of Physics

UNIVERSITY OF
Southampton

Department of Physics and Astronomy
University of Southampton
United Kingdom
April 19, 2021

Modelling the UV and Optical Emission from Accretion Disks around Supermassive Black Holes

Alexander Scott Weston

Abstract

One of the biggest mysteries in modern extra-galactic astronomy is the origin of UV/optical variability in active galactic nuclei (AGN). Although the general consensus amongst the scientific community is that the majority of the variability is likely caused by x-ray reprocessing, we currently lack the evidence to state this for certain. The aim of this project was to help solve this mystery by providing evidence to this x-ray reprocessing argument. This was done by deriving and utilising unique, semi-analytical, non-normalised, response functions from a face-on Shakura-Sunyaev (SS) disk combined with a point-like x-ray corona situated above the central black hole. To produce physical response functions, we found it necessary to include an optical depth factor $\propto \left(1 - \left(\frac{r_{\mathrm{in}}}{r}\right)^{1/2}\right)^{4/5}$ in our heating term to reflect the thinning of the disk at small radii. We then convolved our response functions with x-ray light curves from Seyfert galaxy *NGC 4593* to produce model UV/optical light curves and compared these with real UV/optical light curves from the same galaxy via auto-correlation functions (ACFs). Analysis with ACFs identified that an accretion disk-only response function was not suitable to explain the observed UV/optical light curves due to re-emission timescales being too short. We reasoned the addition of a broad line region (BLR) with a reprocessing timescale of 2-3 days could explain the difference and found evidence in the literature of timescales of BLRs for *NGC 4593* which matched the difference between our model and data ACFs. As an extension to the project, we began analysis of the inclined disk, deriving a new algebraic method for creating semi-analytical, non-normalised, response functions for the inclined disk system. This could become a great potential aid in research into AGN variability.

Declaration

I, Alexander Scott Weston, declare that this dissertation titled *Modelling the UV and Optical Emission from Accretion Disks around Supermassive Black Holes* and the work presented within are my own and have been generated as a result of my own research. I confirm that where I have consulted or quoted the work of others, this is clearly attributed and the source given.

Dedication

I would like to dedicate this dissertation in memory of my maternal grandparents, William Bradshaw (27th May 1927 - 21st November 2018) and Cynthia Bradshaw (26th September 1933 - 23rd December 2020), who both sadly passed away before I was able to complete my degree. They always believed in me and were always proud of my achievements and will be sorely missed.

Acknowledgements

I would like to thank all members of staff who have helped me complete my degree here at Southampton. Sadly there are too many to list but I would like to give a special thanks to my supervisor, Professor Ian M. M$^{\text{c}}$Hardy, without whose advice and guidance this project, and a previous unrelated one, would have both been a great deal more difficult. I also wish to thank my friends and family for their unending support.

Contents

1 Introduction

1.1 Active Galactic Nuclei: A Background

The study of active galactic nuclei (AGN) has been at the forefront of modern research since the 1960s [1]. The source of AGN power is widely believed to be accretion onto supermassive black holes, first independently suggested by Salpeter [2] and Zeldovich [3] in 1964. It was not long before the theory was widely accepted and led to the publication of several fundamental papers in the field, still widely cited today. Arguably, the most important was the publication by Shakura and Sunyaev in 1973 [4] which is known today as the *Standard Accretion Disk Model* or the *α-Disk Model* [5]. Throughout this report, we shall refer to it as the *SS Model*, after the original authors, a common nomenclature in the field of accretion disk physics. The model was fundamental for this project and hence we cover it in detail along with a derivation in section 2.1. A relativistic generalisation of this model was published in the same year by Novikov and Thorne [6]. For the purposes of this project, the latter was deemed an unnecessary complication and we chose not to use it, given that the difference in results produced from the two would be negligible.

AGN have been found to emit across the electromagnetic spectrum, from radio to gamma radiation [7]. It is not uncommon for them to have bolometric luminosities as large as 10^{12} L$_\odot$ and not rare for larger [8], easily outshining all the stars in their entire host galaxy (known as an active galaxy) in the process. In the years since 1973, attempts have been made at explaining the geometry of the extreme environments involved. The current picture, known as the *Unified Model*, consists of a combination of: a small but brilliant x-ray corona [9]; enormous relativistic jets [10]; further-out broad-line regions (BLR) [11]; and dusty tori [12] along with the expansive accretion disk. A diagram of an AGN is shown in figure 1. A common feature of spectra taken from AGN is the *big blue bump* [13], a large excess in flux from AGN in the UV region which is successfully explained using the *SS Model*.

Whilst the formation and evolution of stars is a well-understood subject, the formation of galaxies and AGN are an almost complete mystery [14]. Another mystery is the origin of the UV/optical variability observed in AGN. There are currently two leading theories to explain the observed variability. The first of these suggests that variations in the inflow of accretion material cause variations in the temperature and hence emitted radiation from the disk [15]. The second is that a variable x-ray corona illuminates the disk causing it to heat up and re-radiate [16]. The latter option was the subject of this investigation. For some more in-depth discussion on the details of AGN, see a review such as [17].

1.2 Aims and Objectives of the Project

The main aim of this project was to attempt to model the UV/optical variability observed in AGN. This was to be done by creating an x-ray reprocessing model. The model was then to be used to create response (alternatively known as transfer) functions. We would then use these, along with x-ray, UV and optical measurements of the Seyfert galaxy *NGC 4593* obtained from the *Neil Gehrels Swift Observatory*, to try and explain any possible correlation between the two, and hence provide any further evidence towards validating or rejecting the x-ray reprocessing model. If a strong link was detected, the measured lag between the x-ray and UV/optical light curves could be used to determine the approximate geometry of the AGN region around the central supermassive black hole. This is known as *reverberation mapping* [18]. A lot of this work follows a similar path to that undertaken by works such as [19, 20, 21] which are referenced frequently.
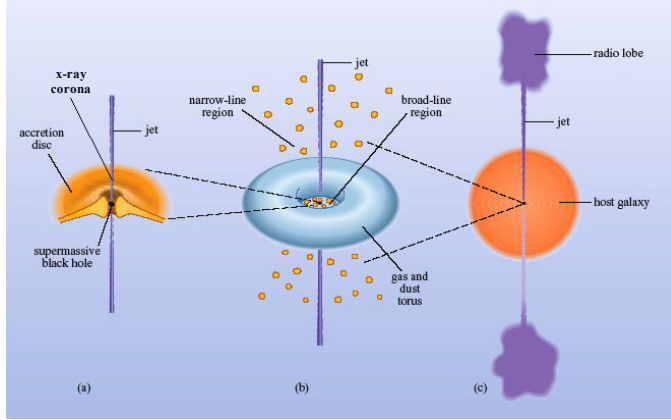
Figure 1: A 'Russian doll' style diagram of a theoretical typical AGN system. (a) The central supermassive black hole is surrounded by an accretion disk and a small but powerful x-ray corona orbiting close by. Relativistic jets sometimes spew out near the top and bottom of the black hole by a very poorly understood mechanism. (b) The broad-line region is sandwiched by the outer accretion disk and inner dusty torus. A narrow-line region is also present but further out and is more diffuse. (c) The jet is very large compared to the host active galaxy, often reaching out many times further than the galaxy's edge forming enormous radio lobes at its ends. It is not uncommon for an AGN's luminosity to swamp its host galaxy's luminosity, making the host galaxy undetectable. Image not created by author. Image credit: Introduction to Active Galaxies. An Open-Learn chunk adapted by permission of The Open University copyright © (2004).

1.3 Target Galaxy: *NGC 4593*

NGC 4593 is a Seyfert galaxy with redshift 0.009 [22] and hence is located close enough to safely ignore cosmological effects such as the expansion of the universe. Seyfert galaxies account for approximately 10% of all galaxies [23] and are intensely studied. When compared with quasars, Seyfert galaxies are much less luminous but both are believed to be powered by accretion. *NGC 4593* has a central supermassive black hole with a mass of about 10^7 suns [24]. Seyfert galaxies are named after Carl Seyfert who first described them in a 1943 paper [25].

2 First Theoretical Model

2.1 The Shakura-Sunyaev Model

2.1.1 Important Details of the Shakura-Sunyaev Model

The *SS Model* is a geometrically thin but optically thick accretion disk model. To eventually fall into the central black hole, orbiting material in the disk must not only lose its gravitational energy, but also its angular momentum. This gravitational energy is converted to heat, the reason that accretion disks are so hot and emit a large portion of their light in the UV (i.e. the origin of the *big blue bump*). The loss of angular momentum turns out to be slightly complicated, however. Although the first disk models were created in the 1940s [26], it took another 30 years for scientists to have a model which could accurately explain the origin of the outward redistribution of angular momentum. It turns out that simple viscosity is not enough to explain the infall and one must add the effects of turbulence in the disk [4]. The *SS Model* relies on the introduction of the parameter α which captures this effect. Although there are no detailed models for this parameter α (and hence it is usually taken constant)[1] [28], we did not need it to proceed with our investigation. We now present a derivation of the important variable Q, equivalent to the heat dissipated per unit area of the disk, and essential for the project. This is a slightly simpler derivation than that by Shakura and Sunyaev [4], but produces the same result.

2.1.2 Shakura-Sunyaev Model Q Derivation

Throughout this derivation (adapted from [29])[2] we make the following important assumptions. First, we assume that the disk is rotationally symmetric about its centre and is most simply described by cylindrical polar coordinates (R, ϕ, z). We assume the disk to be 'steady state' (i.e. the disk's properties are constant with time) and the disk to be thin (i.e. $h(R) \ll R$ where h is the local disk thickness). Furthermore, we assume the viscosity to be small meaning that the disk material's radial velocity is much smaller than its rotational velocity ($v_R \ll v_\phi$). Finally, we use Newtonian mechanics since the *SS Model* is entirely non-relativistic.

The law of mass conservation can be written as:

$$\dot{M} = -2\pi R \Sigma v_R, \tag{1}$$

where $\dot{M}$ is the mass accretion rate onto the black hole and Σ is the mass per unit area on the disk (i.e. $\Sigma = \int \rho(z)\, dz$ with ρ the mass per unit volume). For momentum conservation in the radial direction along with $v_R \ll v_\phi$ we use:

$$v_\phi^2 = (R\,\Omega(R))^2 = \frac{GM}{R}, \tag{2}$$

with G Newton's gravitational constant, M the black hole mass and $\Omega(R)$ the angular velocity at radius R. For the conservation of angular momentum we must take into account the viscous forces. Equation (2) implies differential rotation and allows the required outward transport of angular momentum. Consider two mass elements in the disk A and B' at radial distances R and $R + \lambda$ respectively. Due to the turbulent

---

[1]Fortunately, it is often the case that variables associated with the disk only depend weakly with on α [27].
[2]All credit to Professor Jelle Kaastra of Leiden University.

velocity $\tilde{v}$, the mass elements move outwards to A' and inwards to B respectively. Element A brings its $v_\phi = R\Omega(R)$ to A' where it adds $(R + \lambda)R\Omega(R)$ to the specific angular momentum[3] at the outer radius. Element B' brings its $v_\phi = (R + \lambda)\Omega(R + \lambda)$ to B where it adds $R(R + \lambda)\Omega(R + \lambda)$ to the specific angular momentum at the inner radius. This results in a net transfer of angular momentum from the inner to outer annulus per unit time of $\frac{d\mathcal{L}}{dt} = \dot{M}R(R + \lambda)[\Omega(R) - \Omega(R + \lambda)]$. We hence denote the total scalar torque[4] G that the inner annulus exerts on the outer annulus (by performing an appropriate Taylor expansion and substituting in our values of $\dot{M}$ and v_R) as:

$$G(R) = 2\pi R \Sigma \tilde{v} R^2 \lambda \frac{d\Omega}{dR}. \tag{3}$$

For Keplerian motion ($\frac{d\Omega}{dR} < 0$), the inner annulus loses its angular momentum to the next outermost annulus. Ignoring the inner and outermost annulus on the disk, every annulus has two neighbouring annuli. An annulus located between R and $R + dR$ is subject to a net torque which can be written as $G(R + dR) - G(R) \approx \left(\frac{dG}{dR}\right) dR$. This local change in torque, along with the inward matter flow, allows us to write conservation of angular momentum as:

$$\frac{\partial}{\partial t}(2\pi R dR \Sigma R^2 \Omega) = (2\pi R \Sigma v_R R^2 \Omega(R)) - (2\pi R \Sigma v_R R^2 \Omega(R + dR)) + \frac{\partial G}{\partial R} dR, \tag{4}$$

where we have implicitly ignored second and higher order dR components in the second term. Taking $dR \longrightarrow 0$ and rearranging:

$$R\frac{\partial}{\partial t}(\Sigma R^2 \Omega) + \frac{\partial}{\partial R}(R\Sigma v_R R^2 \Omega) = \frac{1}{2\pi}\frac{\partial G}{\partial R}. \tag{5}$$

It is now we consider the properties of λ and $\tilde{v}$. For a thin disk, the mean free path will never be much larger than h and it is unlikely that $\tilde{v}$ will be supersonic as the subsequent shocks would tend to thermalise the turbulent motion, reducing $\tilde{v}$ back to subsonic. Therefore we can write:

$$\lambda \tilde{v} = \alpha c_s h, \tag{6}$$

where c_s is the (local) speed of sound in the disk and α is the famous parameter from Shakura and Sunyaev. Given our conditions above, we can take $\alpha \lesssim 1$. This is known as the α-condition. Therefore we have:

$$G(R) = 2\pi R \Sigma R^2 \frac{d\Omega}{dR}\alpha c_s h. \tag{7}$$

Often this is equivalently written as:

$$G(R) = -2\pi R^2 W_{R\phi}, \tag{8}$$

where $W_{R\phi}$ is the translational stress integrated over z:

$$W_{R\phi} = \int t_{R\phi}\, dz, \tag{9}$$

and the SS condition is written as:

$$t_{R\phi} = \alpha p, \tag{10}$$

---

[3]For material traversing (nearly) circular orbits, this is velocity times radial distance.

[4]Due to the symmetry of the system, we can safely ignore vector notation without loss of generality. Therefore $G = \frac{d\mathcal{L}}{dt}$.

with p the pressure in the disk. For a stationary flow (i.e. $d\dot{M}/dt = 0$) it follows from (5) that:

$$\frac{d}{dR}(R^3 \Sigma v_R \Omega) = -\frac{d}{dR}(R^2 W_{R\phi}).$$ (11)

Integrating this and substituting (1) we obtain:

$$2\Omega \dot{M} R^2 = 4\pi R^2 W R\phi + C,$$ (12)

with C a constant of integration related to the amount of angular momentum that the disk loses at its innermost annulus. At the inner edge of the disk, we should have $W_{R\phi} \approx 0$. This is because we expect the disk's thickness to approach 0 at the inner boundary and hence from (9), we obtain the required result. We therefore find that $C = 2\Omega_{\text{in}} \dot{M} R_{\text{in}}^2$ where the subscript 'in' denotes the inner edge of the disk. Substituting our equation for C along with (2) into (12) we obtain:

$$W_{R\phi} = \frac{\Omega \dot{M}}{2\pi}\left(1 - \left(\frac{R_{\text{in}}}{R}\right)^{1/2}\right).$$ (13)

To finalise our derivation of Q, we return to considering annuli in the disk. The net torque on an annulus of thickness dR was given by $(\partial G/\partial R)dR$. Multiplying this by Ω gives us the work done by this torque on the rotating annulus per second. This can be written as (using primes to denote differentiation with respect to R):

$$\Omega G' dR = [(\Omega G)' - G\Omega']dR,$$ (14)

where we have used the well-known product rule. It turns out that the term $(\Omega G)'$ represents the convection of rotational energy through the disk caused by the torque and it only depends on the boundary conditions of the disk. The $G\Omega'$ term, on the other hand, represents the dissipation of mechanical energy into the disk material as thermal energy. Per unit surface area of the disk, we can therefore write Q, the heat dissipated through the disk, as:

$$Q = \frac{G\Omega'}{2 \cdot 2\pi R},$$ (15)

where the first factor of 2 in the denominator represents the two sides to the accretion disk. Substituting (8) and (13) into (15) we obtain the desired result:

$$Q = \frac{3GM\dot{M}}{8\pi R^3}\left(1 - \left(\frac{R_{\text{in}}}{R}\right)^{1/2}\right).$$ (16)

This shows that, conveniently, the heat dissipation of the disk is independent of α. Applying the black body assumption $Q = \sigma_{\text{SB}} T^4$, we obtain the temperature profile of the disk:

$$T(R) = \left(\frac{3GM\dot{M}}{8\pi\sigma_{\text{SB}}R^3}\left(1 - \left(\frac{R_{\text{in}}}{R}\right)^{1/2}\right)\right)^{1/4}.$$ (17)

It is important to note that the derivation above has implicitly ignored the effects of strong magnetic fields which can affect the stability of the system and enhance the transport of angular momentum. See, for example, [30, 31] for a more in-depth look at these effects.

2.2 Changing Units

To allow easier comparison between various AGN systems, it is often convenient to change to a different system of units than that of SI. Instead of metres, we wish to measure radii in gravitational radii R_g, masses in kg are converted to solar masses $M_\odot$ and mass accretion rates in kgs^{-1} are converted to Eddington units $\dot{M}_\mathrm{Edd}$. The conversions for these are as follows:

$$R = rR_\mathrm{g} = r\frac{GM}{c^2}, \tag{18}$$

$$M = mM_\odot, \tag{19}$$

$$\dot{M} = \dot{m}\dot{M}_\mathrm{Edd} = \dot{m}\frac{L_\mathrm{Edd}}{\eta c^2} = \dot{m}\frac{4\pi GMm_p}{\eta c\sigma_\mathrm{T}}, \tag{20}$$

where m_p is the proton mass, c is the speed of light in vacuum, η is the accretion efficiency given by (22) and σ_T is the Thomson cross-section. Using this change of variable we obtain a new temperature profile $T(r)$ given by:

$$T(r) = \left(\frac{3m_p c^5 \dot{m}}{2\eta\sigma_\mathrm{T}\sigma_\mathrm{SB}GM_\odot mr^3}\left(1 - \left(\frac{r_\mathrm{in}}{r}\right)^{1/2}\right)\right)^{1/4}. \tag{21}$$

2.3 Small Additions to Shakura-Sunyaev

The accretion efficiency is given by:

$$\eta = 1 - \sqrt{1 - \frac{2}{3r_\mathrm{in}}}, \tag{22}$$

where r_in is equivalent to R_in but has been converted to gravitational units. For an appropriate value of r_in, we chose to use the black hole's innermost stable circular orbit (ISCO). This is because matter inside of this radius will automatically spiral into the black hole over time without any frictional disk process required due to the effects of general relativity. To determine the value of r_in, one must use the black hole's dimensionless spin parameter $-1 \leq a \leq 1$.[5] Bardeen et al. [32] derived the equations for r_in and hence we merely quote the result without the complex derivation (which requires a strong grasp of general relativity and is well beyond the scope of this report):

$$r_\mathrm{in} = 3 + Z_2 - \mathrm{sgn}(a)\sqrt{(3 - Z_1)(3 + Z_1 + 2Z_2)}, \tag{23}$$

where

$$Z_1 = 1 + \sqrt[3]{1 - a^2}\left(\sqrt[3]{1 + a} + \sqrt[3]{1 - a}\right), \tag{24}$$

and

$$Z_2 = \sqrt{3a^2 + Z_1^2}. \tag{25}$$

In equation (23), $\mathrm{sgn}(a)$ is the 'sign' function.[6] When $a > 0$ we are dealing with prograde rotation (meaning that the black hole is spinning in the same direction as the accretion disk) and when $a < 0$ we are dealing

---

[5]Technically, a only varies from 0 to 1. When we take $a < 0$, we are saying that the disk rotates in the opposite direction to the black hole. This 'negative' a is only perceived as negative by the disk in this case.

[6]$\mathrm{sgn}(x) = \begin{cases} 1 & x > 0 \\ 0 & x = 0 \\ -1 & x < 0 \end{cases}$

with retrograde motion (meaning that the black hole is spinning against the rotation of the accretion disk). Crucially, equation (23) tells us that a 'maximally-Kerr' black hole has an ISCO at 1 R_g and a Schwarzschild has an ISCO at 6 R_g. It is unlikely one would encounter a retrograde black hole in nature, except possibly after a black hole-black hole merger [33]. It is likely that most black holes have $a \approx 1$ [34]. A plot of equations (22) and (23) is provided as figure 2. We now have all the equations required to describe the 'unilluminated' accretion disk.
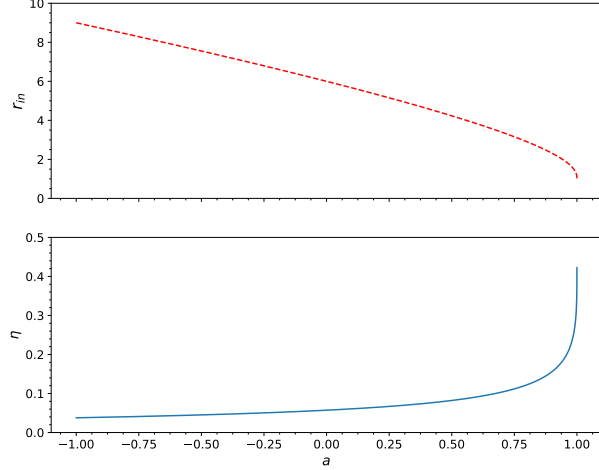

Figure 2: A plot of the ISCOs and Eddington accretion efficiencies for a range of black hole spins. The closer to maximal spin a black hole is, the closer the accretion disk's inner edge can reside to the black hole. As a result, the material can get deeper into the black hole's gravitational well before being inside the ISCO (being unable to contribute to frictional processed) and swallowed up. Hence it can release more of the gravitational potential energy as heat, leading to a higher efficiency. A 'maximally-Kerr' ($a = 1$) black hole's accretion efficiency is 42.2 percent, a Schwarzschild's ($a = 0$) 5.7 percent and a fully retrograde's ($a = -1$) just a measly 3.8 percent.

2.4   Disk Reprocessing Addition to *SS Model*

The next step in creating our model was modelling our disk illumination and the effect it had upon the accretion disk. We chose to model our illumination as a variable x-ray point source of luminosity L_X at a perpendicular (to the accretion disk plane) height $H_\mathrm{X} = h_\mathrm{X} R_\mathrm{g}$ above the black hole. Although a spherical source is likely a more accurate description, the point source approximation is common throughout the field of disk reprocessing. The complications involved in changing the mathematics of a point source to a spherical one are substantial when compared to the increase in accuracy gained. For an example of a spherical source analysis, see [35]. We assumed that our coronal x-ray source's emission was spherically symmetric and hence the flux F_X the disk receives at a distance D_X from our point source is given by:

$$F_\mathrm{X}(D) = \frac{L_\mathrm{X} \cos \Upsilon}{4\pi D_\mathrm{X}^2}, \tag{26}$$

where Υ is the angle between the vector normal to the surface of the disk and the vector drawing a line from the point of interest at radial distance R on the disk to the x-ray source. By Pythagoras' theorem:

$$D_\mathrm{X}^2 = R^2 + H_\mathrm{X}^2, \tag{27}$$

and by elementary trigonometry:

$$\cos \Upsilon = \frac{H_\mathrm{X}}{\sqrt{R^2 + H_\mathrm{X}^2}}. \tag{28}$$

Therefore we obtain:

$$F_{\mathrm{X}}(r) = \left(\frac{c^2}{GM_\odot m}\right)^2 \frac{L_{\mathrm{X}} h_{\mathrm{X}}}{4\pi \left(r^2 + h_{\mathrm{X}}^2\right)^{3/2}}. \tag{29}$$

The effect of the x-ray source on the disk is to add energy to it and therefore heat it. If the disk has an albedo $\mathcal{A}$, we obtain a new effective temperature given by:

$$T_{\mathrm{new}}(r) = \left(T^4(r) + \left(\frac{c^2}{GM_\odot m}\right)^2 \frac{L_{\mathrm{X}} h_{\mathrm{X}}(1 - \mathcal{A})}{4\pi\sigma_{\mathrm{SB}} \left(r^2 + h_{\mathrm{X}}^2\right)^{3/2}}\right)^{1/4}, \tag{30}$$

with $T(r)$ defined as equation (21). We chose to assume a constant albedo of 0.3 throughout the remainder of the study, a value suggested by [36] and what appears to be the 'go-to' value. In reality, albedo varies with x-ray photon energy [37] but the effect is small when compared with other uncertainties involved and the constant albedo approximation is common.[7] A paper by Rokaki and Magnan [39] attempted a similar model to us except they attempted to model line and continuum emission of the disk from x-ray reprocessing instead of broad-band UV/optical emission.

2.5 Model Tools and Practicalities

All models were constructed in *Python 3.7* using the *Anaconda* package. As analytical integration was impossible given the forms of $T(r)$, all integration was numerical using *Simpson's rule*. To ensure maximal accuracy, we modelled our accretion disk as 1000 logarithmically-spaced annuli. This ensured maximum precision at small radii where the temperature varied most but also allowed us to cover wide areas of the outer disk quickly where temperature variation, and hence flux variation, was small. Our code for our final response function model is placed in the appendix in section C.

---

[7]See, for example, [19, 20, 38] for alternative examples of the constant albedo approximation.

3 Application of First Model

3.1 First Model Temperature Profiles and Spectra

The next part of our project was to calculate and plot disk temperature profiles and disk spectra for both the illuminated and non-illuminated cases. We provide a plot of equations (21) and (30) as figure 3a. To calculate the spectrum of the accretion disk, we first needed Planck's famous black body function:

$$B_\nu(T) = \frac{2h\nu^3}{c^2} \frac{1}{\exp\left(\frac{h\nu}{k_B T}\right) - 1},$$ (31)

where h is the Planck constant, k_B is the Boltzmann constant and ν is the frequency. The Planck function has units of $\mathrm{Wm^{-2}Hz^{-1}Sr^{-1}}$.[8] By integrating over the whole accretion disk, and making sure to account for the radial dependence of temperature, one obtains the spectrum of the accretion disk:

$$L_\nu = 2\pi \int_{r_{in}}^{r_{out}} B_\nu(T(r)) \, 2 \cdot 2\pi r \left(\frac{GM_\odot m}{c^2}\right)^2 dr,$$ (32)

where the first factor of 2π comes from each side of the disk emitting over half of physical space, the second factor of 2 comes from the two sides of the accretion disk and the final factor of 2π comes from an infinitesimal area element on the disk. The spectrum of an accretion disk has a very distinct three-segment shape as shown in figure 3b.

3.2 Generating Response Functions from the First Model

3.2.1 Physicality of Response Functions

The next task was to generate response functions. Before we present this derivation, it is important that the reader understands what a response function is. In our case, it is the behaviour of the steady-state unilluminated accretion disk as it responds to a Dirac-delta impulse of x-ray radiation from our point source. When the point source emits, the wave of radiation travels outwards at the speed of light, heating parts progressively further from the black hole. Accretion disks around supermassive black holes easily out-scale the solar system [41], meaning the wave of illumination can take a few days to reach the outer edges of the disk. As the different parts of the disk are heated, they re-emit which we model as black body radiation. The majority of this re-emission will be in the UV/optical bands. As a result, there is a time-dependent extra emission from the disk which evolves as a function of time due to the x-ray flux falling off with distance. For the face-on disk, the time delay (and hence response) is simply a function of the radial coordinate on the disk by rotational symmetry. If the disk is inclined, however, the delay and response depend on the angular coordinate as well and is substantially more complicated to calculate (the subject of section 7). Once we have a response function, we can convolve it with a real x-ray light curve to predict the corresponding UV/optical light curves.

---

[8]One must take care to ensure the 'per-steradian' part of the units are dealt with correctly.
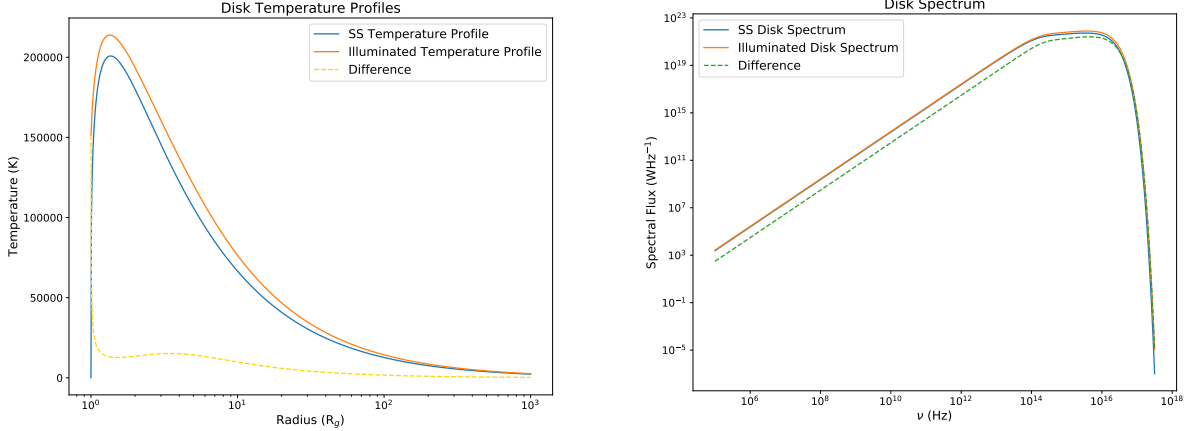
(a) The temperature profiles for an example black hole and their difference. The plot uses $m = 5\text{x}10^7$, $\dot{m} = 0.05$, $r_{out} = 10^3$, $a = 1$, $L_X = 8\text{x}10^{10}$ $L_\odot$, $h_X = 3$ and $\mathcal{A} = 0.3$. These values are similar to a 'typical' AGN such as NGC 4593 [19, 40]. The illuminated disk is hotter as one would expect given the extra energy being added to the disk. The plot also highlights the importance of the addition of the $1 - \left(\frac{r_{in}}{r}\right)^{1/2}$ term. Without this term, the innate disk temperature follows a $1/r^3$ dependence and grows to unphysically large values at small radii close to the black hole. The dashed yellow line shows the difference between the two temperature profiles. It is very large at small radii, something that we later found to be unphysical resulting in a necessary model adaption, the subject of section 4.

(b) The spectra of the temperature profiles in figure 3a along with their difference. There is a clear peak in the UV as we would expect (i.e. the big blue bump). The relative difference between the two appears quite small but the logarithmic plot can be deceiving. The x-ray source has the effect of adding over 50 percent to the output of the accretion disk with the given parameters. The total luminosity of the disk increases from $1.94\text{x}10^{11}$ $L_\odot$ to $3.00\text{x}10^{11}$ $L_\odot$. This non-negligible effect allowed us to construct physical response functions. The plot also clearly demonstrates the characteristic three-segment spectra of accretion disks. At lower frequencies, the spectral flux grows as ν^2 before transitioning to $\nu^{1/3}$ and then to $\nu^2 \exp\left(-\frac{h\nu}{k_B T}\right)$. A derivation of these behaviours is presented in [27].

Figure 3: Both plots use the same parameters.

3.2.2 Face-on Disk Response Function Calculation

As we are interested in the extra radiation (the difference plotted in figure 3b), it is helpful to first introduce a quantity $\Delta B_\nu(r)$ defined as:

$$\Delta B_\nu(r) = B_\nu(T_{\text{new}}(r)) - B_\nu(T(r)). \tag{33}$$

One then naturally chooses to use this to define $\Delta I(r)$:

$$\Delta I(r) = 2\pi \int_{\nu_{\text{min}}}^{\nu_{\text{max}}} \Delta B_\nu(r) \, d\nu, \tag{34}$$

where ν_{min} and ν_{max} are the lower and upper bounds of the frequency range one is interested in and the 2π, as before, refers to integration over half of physical space. If one wanted to cover all frequencies, one would technically put $\nu_{\text{min}} = 0$ and $\nu_{\text{max}} \longrightarrow \infty$. However, one can see from figure 3b that beyond a very small range around the peak, the spectral flux is negligible and can be safely ignored.

With the face-on disk, the extra time taken for light to travel[9] from the x-ray source and hit the disk before travelling back towards the observer (hereafter referred to as the lag τ) can, assuming an observer at

---

[9]When compared with the time taken for light to travel directly from the x-ray source to the observer.

infinity, be defined as:

$$\tau(r) = \frac{GM_\odot m}{c^2} \frac{\sqrt{h_X^2 + r^2} + h_X}{c}. \tag{35}$$

The next step is to divide our disk into rings of width dr. We then wish to consider the total extra radiation emitted by an annulus due to the heating:

$$dP(r) = 2 \cdot \Delta I(r) 2\pi \left(\frac{GM_\odot m}{c^2}\right)^2 r dr. \tag{36}$$

This (two-sided) annulus will emit its radiation over a period of time given by the difference in time for the x-ray radiation to reach the inner and outer edges of the annulus:

$$\frac{\Delta L(r)}{\Delta \tau} = \frac{dP(r)}{\tau(r + dr) - \tau(r)}. \tag{37}$$

Taking the limit as $dr \longrightarrow 0$ we obtain the definition of our response function:

$$\frac{\partial(\Delta L(r))}{\partial \tau} = 2 \cdot \Delta I(r) 2\pi \left(\frac{GM_\odot m}{c^2}\right)^2 r \frac{dr}{d\tau}. \tag{38}$$

The only thing left to calculate is the derivative of r with respect to τ. This is simple as τ is a function of r only. We calculate this as follows:

$$\frac{dr}{d\tau} = \left(\frac{d\tau}{dr}\right)^{-1} = \frac{c^3}{GM_\odot m} \frac{\sqrt{r^2 + h_X^2}}{r}. \tag{39}$$

We now write the definition of our response function used in our code where we have explicitly written out terms where appropriate for ease of replication:

$$\frac{\partial(\Delta L(r))}{\partial \tau} = 2 \cdot 2\pi \frac{GM_\odot m}{c} \sqrt{r^2 + h_X^2} \, 2\pi \int_{\nu_{\min}}^{\nu_{\max}} [B_\nu(T_{\text{new}}(r)) - B_\nu(T(r))] \, d\nu, \tag{40}$$

where the different factors of 2 are the same as described below equation (32). This equation represents the extra luminosity of the disk per second when heated by an impulse of x-ray radiation centred on the x-ray point source. One then plots this as a function of $\tau(r)$. It is easy to check (numerically) that the area under the response function defined above is equal to the area under the difference disk spectrum indicating that we have performed our analysis correctly. The result is exciting as it is not normalised, giving us an idea of the size of our real response. If one wishes to compare this to observations from a telescope, they simply must convert luminosity per second to flux per second by dividing by $\{4\pi(\text{AGN-Earth Distance})^2\}$ and multiply the integrand of equation (40) by their telescope's normalised sensitivity curve over the frequency range.

Unfortunately, the model we have explained above produces unphysical response functions. As the impulse of x-ray illumination travels outwards, the total disk area being hit should grow proportional to r (i.e. $dA \propto 2\pi r dr$). However, as the wave of illumination travels further from the original source, the flux hitting the disk falls off as $(r^2 + h_X^2)^{-3/2}$. As a result, given that accretion disks get quite close to the black holes that they are orbiting, we expect the response function to rise quickly then fall off slowly. The temperature profiles described by equations (21) and (30) produce response functions which start at a high value and fall

off rapidly, hereafter referred to a 'banana' shape. This is clearly unphysical. As an alternative analysis, if our impulse of radiation had, for example, a width dx, then the maximum proportion of area illuminated in each annulus would be proportional to $\frac{dx}{dr}$. When the wave of illumination hit the innermost annulus, this area would be smaller as only a fraction of dx would be touching the disk. Hence he would expect a rise and fall in the response function. From both of these interpretations, it was clear that we were required to adapt our model. A plot of our first model's response function is included in figure 5. Interestingly, if we ignore the $1 - \left(\frac{r_{\text{in}}}{r}\right)^{1/2}$ term, this problem is not present and this gave us a clue to the issue's solution

4 Improved Theoretical Model

4.1 Reasoning

We now had a theoretical physical reasoning to back a modification to our model. For robustness, it was important to identify the mathematical cause of the banana shape. After a thorough investigation, the cause was found to be the difference temperature profile, clearly portrayed in figure 3a. The difference curve behaves well past about 1.5 R_g in the example but inside of this it does not. The temperature difference changes by an order of magnitude over a very small (relative) distance. This occurs because of the $1 - \left(\frac{r_{\text{in}}}{r}\right)^{1/2}$ term in the *SS Model* which pushes the temperature of the accretion disk to 0 K at the inner edge. However, the illuminated disk model does respect this, leading to the large unphysical temperature increase at small radii. It was therefore necessary to 'damp' the illumination function at small radii so that the temperature increase was less substantial.

4.2 The Fix

In the end, we found inspiration from [27]. They extend the *SS Model* beyond what we derived in section 2.1.2 to include the effects of optical depth. By simple radiative transfer theory one can work out the total absorbed flux which is used to heat the disk. Therefore, we can make the following substitution in equation (30):

$$L_{\text{X}} \longrightarrow L_{\text{X}} \left(1 - \exp(-\chi(r))\right), \tag{41}$$

where χ is the perpendicular optical depth of the accretion disk at a radius r. To find a functional form for χ we again consult [27]. They give a functional form which we can take as the following:

$$\chi = \chi_0 \left(1 - \left(\frac{r_{\text{in}}}{r}\right)^{1/2}\right)^{4/5}, \tag{42}$$

where χ_0 is a function of α of order 1 left as a free variable.[10] The term χ compensates for that, in reality, the accretion disk will thin and decrease in density at small radii (taken from the equations labelled as (5.49) in [27]). As a result, the optical depth decreases and therefore x-ray photons are more likely to pass through the disk without interacting with it. We now define the illuminated temperature profile as:

$$T_{\text{new}}(r) = \left(T^4(r) + \left(\frac{c^2}{GM_\odot m}\right)^2 \frac{L_{\text{X}} h_{\text{X}}(1 - \mathcal{A})\left(1 - \exp\left(-\chi_0\left(1 - \left(\frac{r_{\text{in}}}{r}\right)^{1/2}\right)^{4/5}\right)\right)}{4\pi\sigma_{\text{SB}}\left(r^2 + h_{\text{X}}^2\right)^{3/2}}\right)^{1/4}. \tag{43}$$

All other previously stated variables remain the same. The temperature and thus black body flux of the illuminated disk now drops to 0 at r_{in}. A plot of the new temperature profiles is provided as figure 4a along with a surface brightness comparison as figure 4b. The disk spectrum from the new temperature profiles is negligibly different from that shown in figure 3b.

---

[10]Simulations would be required to find a more accurate bound on χ_0.
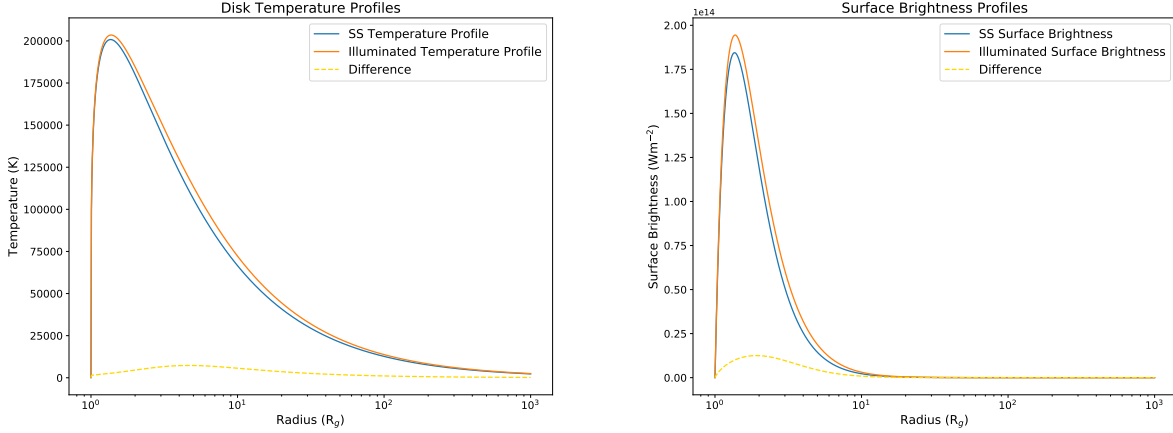
(a) A plot of our new temperature profile with the inclusion of the optical depth term.

(b) A plot to show the surface brightness profile of the accretion disk with our new temperature profile.

Figure 4: Both plots use the same parameters as figure 3 with the addition of $\chi_0 = 1$. The surface brightness profile is much more peaked when compared to the temperature profile, as we would expect, due to the T^4 dependence of the Stefan-Boltzmann law.

4.3 Response Function Analysis and Comparison

We provide a comparison of both our first and second attempts at response functions, with the same parameters, in figure 5. It was helpful to vary some of the parameters used in forming figure 5 to understand how they affected the shape and size of the response function. We present a selection of parameter variations to give the reader an understanding of this as figure 6.

Our response functions now matched the functional form of those found elsewhere in the literature (for example see [20]). It was at this point we decided to advance with the project.
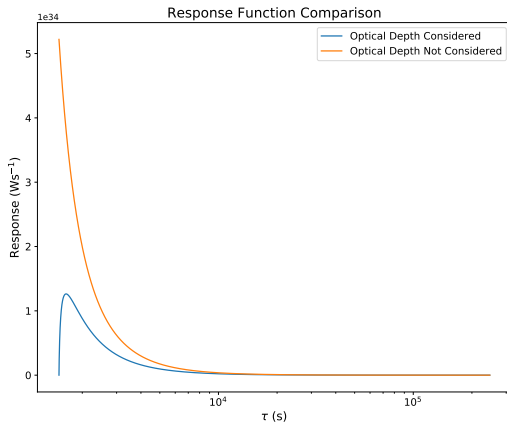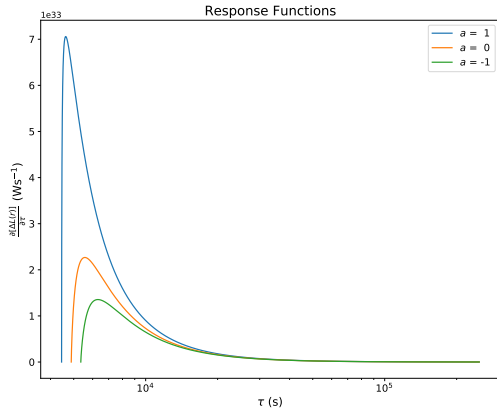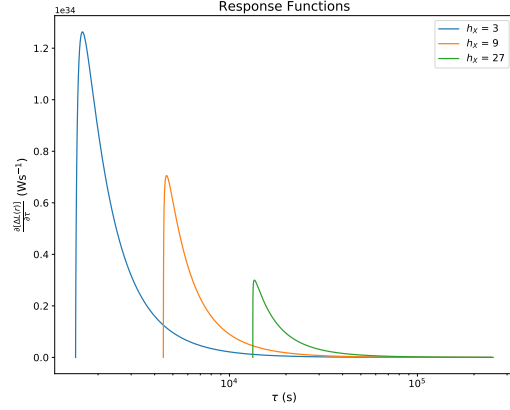

Figure 5: A plot to compare the effects of including (with $\chi_0 = 1$) and ignoring the optical depth. The optical depth has a clear effect on preventing the formation of a 'banana' response function which for the reasons described in section 4.1 is unphysical. In the plot we have used the response function of the whole electromagnetic spectrum. Inclusion of optical depth produced response functions that agree with those in other papers such as [19, 20]. The plot also clearly shows that, as one would expect, almost all of the disk's response is in the inner regions of the disk where the x-ray flux is greatest. An important feature common to both versions of our responses is that they do not start at $\tau = 0$. They start at the time corresponding to $\frac{GM_\odot m}{c^2} \frac{\sqrt{r_{in}^2 + h_X^2} + h_X}{c}$, the shortest extra distance an x-ray could travel to the disk and back towards the observer.

18

(a) A plot to compare the effects of varying black hole spin on the response function. This plot uses the same parameters as figure 4 except for $h_X = 9$. This has to be done because of the ISCO bound on the position of the x-ray point source. Previously, we took $h_X = 3$ but this only works for spin-1 black holes. The plot agrees with our intuition. Higher spin black holes have closer inner edges of their accretion disks which receive larger amounts of x-ray flux thus their responses are greater and earlier. A subtlety is that as $\dot{m}$ varies with accretion efficiency, it also varies with spin which affects the plot by slightly amplifying the responses of black holes with spins less than +1. This can be seen by substituting the definition of η into T and T_{new}.

(b) A plot to compare the effects of varying the height of the x-ray source on the response function. This plot uses the same parameters as for the spin-1 black hole described in figure 4 except for the varying x-ray source height. An accretion disk with a higher companion x-ray source will have a smaller peak x-ray flux on the disk and the radiation from an impulse will take longer to reach the disk. Perhaps surprisingly, the total extra disk luminosity (area under the graphs) increases slightly with (small) x-ray heights due to the larger value of h_X in the $\cos \Upsilon$ term. Physically, this means the angle Υ is smaller so the x-ray radiation hits the disk at less of an angle. Although the peak flux for larger h_X is smaller, it falls off slower with increasing r. For heights of order 100 R_g and larger, it begins to decrease again.

Figure 6: A pair of plots of response functions with varying parameters. We chose to demonstrate varying spin and x-ray source height as other parameters are easier to constrain with current observations [19, 40].

5 Data

Our data is identical to that first used by McHardy et al. [21] and was provided to us by Ian M. McHardy for this project. It was collected by the *Neil Gehrels Swift Observatory* in an observing session on Seyfert galaxy *NGC 4593* performed over a period of ~ 23 days in mid-July to early-August 2016. The observations were multi-wavelength, with x-ray observations performed by the *X-Ray Telescope* (XRT, [42]) and UV and optical observations performed by the *UV and Optical Telescope* (UVOT, [43]). When we received the data, all necessary steps to reduce the data as described on the NASA Swift website had already been performed. We thank Ian M. McHardy for providing us with the data and performing the necessary data reduction steps for us. A more thorough analysis of the data itself can be found in [21]. We provide a plot of our light curves as figure 7. A discussion of the filter calibrations can be found in [44, 45]. We reproduce a table of the filter central wavelengths and FWHMs of *UVOT* as table 1 and some information about *XRT* as table 2. In figure 8, we provide expected response functions from the different wavebands available using Swift. Other than varying the frequency ranges, all model parameters are the same as previously used in figure 4.

Filter	Central Wavelength (Å)	FWHM (Å)
W2	1928	657
M2	2246	498
W1	2600	693
U	3465	785
B	4392	975
V	5468	769

Table 1: A table of the central wavelengths and FWHMs of the 6 filters available on the UVOT *aboard Swift. Data taken from [44].*

	Energy Range	Effective Area	Sensitivity
XRT	0.2-10 keV	110 cm^{-2} @ 1.5 keV	8 x 10^{-14} ergcm^{-2}s^{-1} in 10^4 s

Table 2: A table of some of the properties of XRT. Data available from the NASA Swift website.
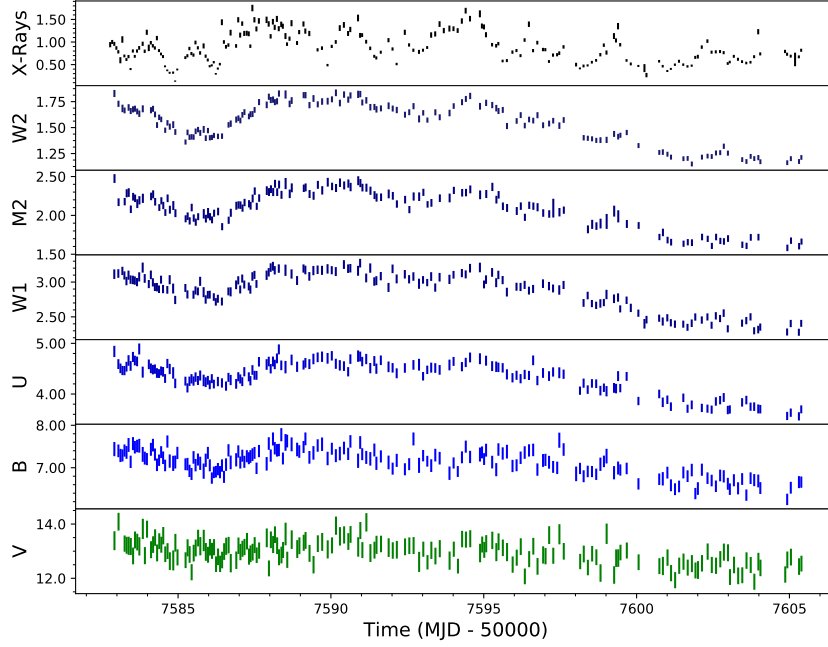
Figure 7: A plot of the 7 light curves we had access to for the study. The units on the y-axis for the x-ray light curve are the 0.5-10 keV count rate. For the other light curves, the units on the y-axis are mJy. When compared to the predicted light curves in figure 9, the real light curves are a lot less variable. Visual inspection of these light curves identified shorter timescale variability in higher frequency wavebands. This is what we would expect from an AGN with x-ray reprocessing causing emission of lower frequency radiation. It should be noted that by-eye the V band appears potentially unreliable as we would expect more variation than present in it. A discussion of this is presented in section 6.2.2.
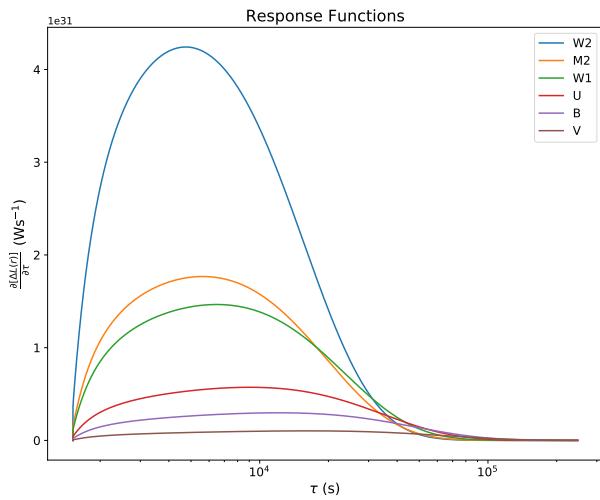

Figure 8: A plot of the 6 response functions produced using the 6 different filters of UVOT with our model. All other model parameters are the same as used in figure 4. In the plot, we have assumed constant sensitivity over the wavelength ranges corresponding to $\lambda_{peak} \pm \frac{FWHM}{2}$. The plot shows what we would expect with emission following Wein's Displacement Law. All of the wavebands in this example are at larger wavelengths than the peak emission wavelength of the model disk. Therefore, bands with smaller corresponding wavelengths are more peaked and move inwards to hotter parts of the disk. For much shorter wavelength photons, the peak emission will drop as expected. Some of the peculiarities in the shapes of the responses are down to the varying sizes of the FWHM of each band.

6 Modelling the Theoretical Link Between X-Ray and UV/Optical Variability

6.1 Convolution of Light Curves and Response Functions

Now that we had a theoretical model which produced reasonable light curves, it was time to test them. The idea was to convolve our response function $\frac{\partial(\Delta L(t))}{\partial \tau}$ with our x-ray light curve $X(t)$. Mathematically, this can be written as:

$$\psi(t) = \int_{\tau_{\min}}^{\tau_{\max}} \frac{\partial(\Delta L(\tau))}{\partial \tau} X(t - \tau) \, d\tau, \tag{44}$$

where $\psi(t)$ is our predicted (optical or UV) light curve as a function of time t, and $\tau_{\min}$ and $\tau_{\max}$ are the lower and upper bound respectively of where our response function is defined. The bounds depend on the geometry and size of the AGN being modelled. Outside of these bounds, $\frac{\partial(\Delta L)}{\partial \tau} = 0$. This is the standard approach in the field (see for example [19, 20]). At this point we found it was necessary to normalise the light curves and response functions to proceed. A good extension to this project would be designing and implementing a convolution algorithm which correctly produces physical outputs from real light curves and our non-normalised response functions. Doing so would allow a more accurate measurement of the distance to *NGC 4593*, currently estimated to be 44±1 Mpc from Earth [46]. Previous papers such as [47] estimated the distance to be closer to 38 Mpc, a relative difference of about 15 percent. A plot of convolution of the x-ray light curve shown in figure 7 with the response functions from figure 8 is shown as figure 9.
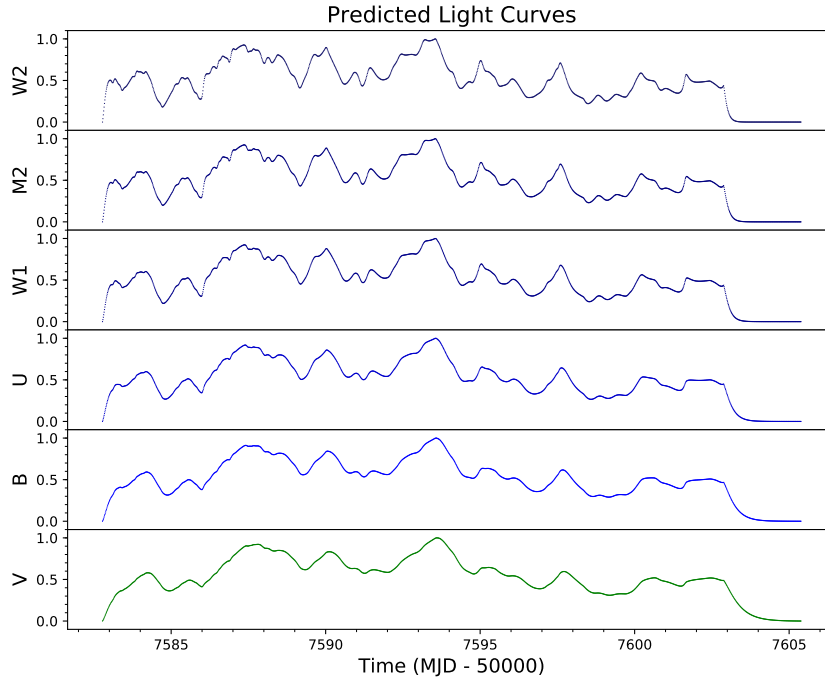

Figure 9: *A plot of our x-ray light curve from figure 7 convolved with the respective response functions from figure 8. The y values are self-normalised to peak due to the reasons discussed in section 6.1. It is important to note the tails on the right sides (and to a lesser extent the left sides) of our plots. These are due to the long tails in our response functions which start and end at close to zero. If one had a light curve of infinite length, these would not be present. Going forward, these were removed from our predicted light curves but are left here to demonstrate the effect of the tail. When r_{out} is allowed to be much larger than 10^3, the tails can grow very large due to the relative weak response of the disk at large radii.*

Due to the nature of *Numpy's* convolution algorithm, both inputs $\frac{\partial(\Delta L)}{\partial \tau}$ and X must be evenly (temporally) sampled. This presented an immediate problem as due to the nature of observational astronomy, this is practically impossible. In addition, due to the non-linear nature of our model's distribution of lags, our response function was also not linearly sampled. To deal with this, we were presented with a couple of

options. The simplest option was to linearly interpolate between each data point. Interpolation is often a risky step but fortunately, the data was not too noisy and sampled often enough that linear interpolation was likely to be acceptably accurate. To ensure equally placed data points for use in convolution we applied the following formula:

$$\frac{t_{\max,\mathrm{R}} - t_{\min,\mathrm{R}}}{N_{\mathrm{R}}} = \frac{t_{\max,\mathrm{X}} - t_{\min,\mathrm{X}}}{N_{\mathrm{X}}}, \tag{45}$$

where the subscript R refers to variables corresponding to the response function and the subscript X refers to variables corresponding to the x-ray light curve, $t_{\min}$ and $t_{\max}$ refer to the first and last times in each data set, and N_{X} refers to the number of data points one wishes to have in their interpolated data sets. To apply equation (45), we chose to pick N_{R} to be equal to 200. There is the potential for equation (45) to produce non-integer values of N_{X}, but in this case if N_{R} is chosen to be large enough, one can just take the floor of the fractional value as the relative error in the differences in sampling between the response function and x-ray data would be negligible.

6.2 Quantifying the Accuracy of the Model

6.2.1 The Discrete Cross-Correlation Function

We now needed a way to quantify comparison of our real and theoretical light curves which we had produced. The most practical way of doing this was with cross-correlation [19]. As any cross-correlation would be with discrete data rather than continuous, it was necessary to consult [48] to formulate how to do so. The method first used by [48] is now commonplace in the field of astronomy due to unevenly sampled data being a common occurrence. To calculate the discrete cross-correlation function (DCF) one proceeds as follows. Given two data trains a_i and b_j, we collect the set of unbinned discrete cross-correlations:

$$\mathrm{UDCF}_{ij} = \frac{(a_i - \bar{a})(b_j - \bar{b})}{\sqrt{(\sigma_a^2 - e_a^2)(\sigma_b^2 - e_b^2)}}, \tag{46}$$

for each possible pair of data points (a_i, b_j). In the above equation, $\bar{a}, \bar{b}$ refer to the mean values of the two time series, σ_a, σ_b refer to the standard deviations of each time series and e_a, e_b refer to the measurement errors associated with each data set. For small e_a and e_b, equation (46) is replaced by:

$$\mathrm{UDCF}_{ij} = \frac{(a_i - \bar{a})(b_j - \bar{b})}{\sigma_a \sigma_b}, \tag{47}$$

where each data point has an associated pairwise lag Δt_{ij} defined as:

$$\Delta t_{ij} = t_j - t_i. \tag{48}$$

For our purposes, equation (47) was more appropriate as e accounts for the variability in a data set (say, for example, a sample of galaxies of varying brightness). Binning the UDCF into equally-sized time bins allows the directly useful function DCF to be measured. Given bins of width $\Delta\tau$, the $\mathrm{DCF}(\tau)$ is defined as the mean over the total UDCF_{ij} with associated Δt_{ij} in the range $\tau - \Delta\tau/2 \leq \Delta t_{ij} \leq \tau + \Delta\tau/2$, akin to a running average. The common approach is then to take the standard deviation of the data points in each bin, divide by the square root of the number of data points in the bin and use this as the error on

the mean of the associated bin. When one takes $a = b$, we have an auto-correlation function (ACF). These are symmetric and peak at $\tau = 0$.[11] Creating ACFs for two different time series and comparing them is an excellent way of understanding if the two time series' variability is of similar timescale. Choosing bin size is a "trade-off between desire for high accuracy in the mean and a counter-desire for resolution in the description of the cross-correlation curve" [48]. Fortunately, it turns out that results only vary weakly with bin size [48].

6.2.2   Applying the Auto-Correlation Function to our Data

As a first-order approximation, assuming that the shapes were broadly similar, we attempted to quantify the similarity of our model light curves and real light curves by the widths of their ACFs. To more accurately identify the best fitting lags and errors on those lags, it would have been necessary to perform simulations. Due to time constraints, this was not feasible but would present a good extension to the project. A plot of our ACFs for both predicted and measured light curves is shown as figure 10.
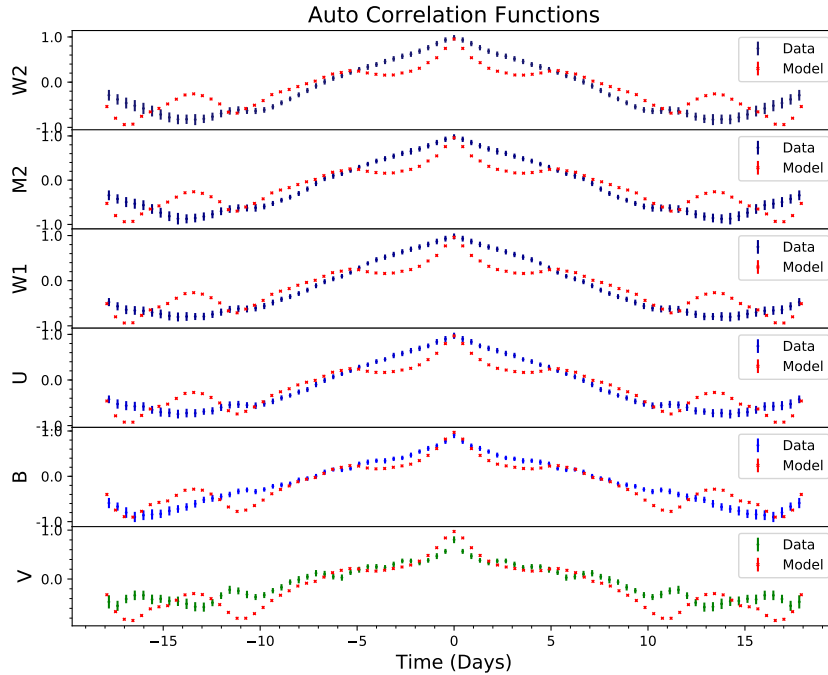

Figure 10: A plot of our predicted and measured ACFs for each band. The data used as inputs is the same as in figures 7 and 9 although the tails have been removed from the latter. The reasoning for this is explained in the caption of figure 9. The V band data ACF does not quite reach 1 due to the non-negligible bin width. Finer binning moves the peak towards 1 at the expense of a noisier ACF. The error bars represent the standard error (and hence a lower bound) on each bin's data and are likely an underestimate, especially for the model ACFs. A table of widths of the ACFs is provided as table 3.

Figure 10 shows our model to have, by-eye, a reasonable fit considering the model's simplicity. However, there are some clear differences between our data and model ACFs. For all bands except V, the model ACF initially falls off too quickly. This means our short timescale reprocessing ($\sim$ 2-3 days) is too variable and potentially needs an extra component such as a BLR. This is discussed in more detail in section 6.3. Our mid-range timescale reprocessing ($\sim$ 5-7 days) is very similar, indicating our response functions are suitable around this delay. For the longer-range timescale reprocessing ($\sim$ 7-10 days), the fit in the four most energetic bands is good. In the less energetic bands, however, there is an underestimate of the ACF in our model. This could possibly be interpreted as yet another reprocessing component. This interpretation has to be performed carefully, however, as the further from the peak of the ACF the less accurate it is due

---

[11]It is possible for (quasi)-periodic functions to have peaks larger than the one at $\tau = 0$ but this does not apply here.

to less data-overlap. Given the length of our light curves, at ~ 10 days the accuracy of the measured ACFs was diminished and hence we did not analyse these outer parts further. An important point to note is that it is very plausible that the V band (and to a lesser degree the B band) light curve is quite poor quality (and hence less significant) when compared to the other bands and hence must be taken with a pinch of salt. As a quantitative tool in such a situation, we utilised the fractional variability of a light curve, introduced by Vaughan et al. [49]. This is defined as:

$$F_{\text{var}} = \sqrt{\frac{S^2 - \bar{\sigma}_{\text{err}}^2}{\bar{x}^2}}, \tag{49}$$

where S^2 is the sample variance, $\bar{x}^2$ is the sample mean squared and $\bar{\sigma}_{\text{err}}^2$ is the mean square error defined as:

$$\bar{\sigma}_{\text{err}}^2 = \frac{1}{N} \sum_{i=1}^{N} \sigma_{i,\text{err}}^2, \tag{50}$$

for a sample of N data points with individual measurement errors $\sigma_{i,\text{err}}$. Calculation of F_{var} is common in time-domain astronomy as a tool to help understand the variability in a light curve. Quoting results from M$^{\text{c}}$Hardy et al. [21], they give the F_{var} of the V-band light curve as 0.024 whilst, for example, F_{var} of the UVW2 light curve is given as 0.125. Although we would expect the V-band light curve to have less variability when compared to the other bands in this study if powered by reprocessing, given the value of F_{var} is so small for the V-band light curve when compared with the other light curves,[12] we concluded it was likely an unreliable data set.

		FWQM (Days)	FWHM (Days)	FW3QM (Days)
W2	Data	6.01 ± 2.92	12.58 ± 2.28	16.97 ± 1.82
	Model	2.28 ± 1.38	14.56 ± 2.47	20.20 ± 1.75
M2	Data	6.68 ± 2.82	13.17 ± 2.33	17.26 ± 2.21
	Model	2.30 ± 1.35	14.43 ± 2.50	20.06 ± 1.62
W1	Data	6.92 ± 2.64	11.72 ± 2.33	16.98 ± 2.40
	Model	2.32 ± 1.33	14.29 ± 2.53	19.91 ± 1.50
U	Data	6.17 ± 2.40	11.88 ± 2.21	16.67 ± 2.42
	Model	2.38 ± 1.28	14.03 ± 2.50	19.53 ± 1.33
B	Data	4.58 ± 3.06	14.20 ± 2.77	23.97 ± 3.44
	Model	2.44 ± 1.21	13.71 ± 2.29	19.11 ± 1.34
V	Data	1.88 ± 1.35	10.85 ± 1.54	18.58 ± 1.56
	Model	2.49 ± 1.14	13.21 ± 2.02	18.41 ± 1.47

Table 3: A table of our full-width quarter maxima (FWQM), full-width half maxima (FWHM) and full-width three-quarter maxima (FW3QM) of our ACFs. An estimate of the error in the table was calculated as the difference in the ACF width at ± 0.05 the associated width (for example 55 percent and 45 percent for the FWHM). Although not a rigorously mathematical calculation of the exact uncertainty, it was deemed a reasonable estimate of the error for comparing different ACF widths. This was because when the ACF was flatter, there was a larger uncertainty in the width than if the ACF was close to vertical. Hence relative errors could be compared between widths. Full width maxima (FWM) were not taken due to the lack of certainty in the accuracy of our ACFs near the extrema due to the lack of data overlap at these regions.

To try and explain the shorter timescale dissimilarity, we first tested the model with increased x-ray source height. The idea was that x-rays from a corona at a greater height above the black hole would take longer to reach the disk. Therefore, the associated response function would be over a longer timescale, widening our ACFs. We found this had negligible improvement upon the ACFs. A second suggested idea

---

[12]Which is visually apparent in how 'smooth' but 'noisy' it appears by eye.

was that the black hole was close to Schwarzschild and had no (or negligible) spin. Due to the behaviour of equation (23), this would mean that the inner disk was further out and hence the timescales associated with reprocessing would be slightly longer. The associated ACFs with this were slightly wider but the difference was small and since most black holes are expected to be near spin 1 [34], the idea was also rejected. Using a retrograde black hole instead also had minimal effect.

Increasing the central black hole mass to 10^8 M$_\odot$ had promising results in higher energy wavebands. However, papers such as [24] estimated the mass to be an order of magnitude lower than this and there was no noticeable improvement in the lower energy wavebands. We therefore rejected modifying the mass parameter. Increasing/decreasing $r_{\rm out}$ tended to broaden/shrink the general form of the model ACF respectively and was hence unhelpful. Hence we believe 5×10^7 M$_\odot$ and 10^3 R$_{\rm g}$ were reasonable estimations of the real system parameters.

6.3 Additional Reprocessing Components

The idea of BLR reprocessing was investigated (although not the first instance of study on this topic) in [21], a similar study to ours with the same data and had promising results. Their study utilised MEMECHO, a maximum entropy fitting method which finds a best fitting response function to explain the observed UV/optical light curves based on the given x-ray light curve. Whilst this technique is effective for finding response functions, it doesn't provide any physical basis for these responses; any physical basis must be interpreted by the user. They reasoned that response timescales of order a few days could be interpreted as reprocessing from a BLR. M$^{\rm c}$Hardy et al. were not the only group to come to this conclusion. One of the first papers theorising BLR reprocessing of x-rays was by Korista and Goad [50]. They found that the addition of an extra, slower, response component to the disk would fit the data well with a wavelength dependent lag $\tau \propto \lambda^{4/3}$. This is consistent with a range of newer studies. In their paper, figure 4 shows a gradual rise in expected flux before a drop due to absorption line effects (clumped as one drop rather than many due to lack of sensitivity) as we would expect from similar reasoning to the disk response's rise and fall. They performed a very similar study on *NGC 5548* in [51] and found comparable results. Another paper on *NGC 5548* [52] found 'longer than expected' lags, consistent with a BLR explanation. A previous paper by Baarth et al. [53] found emission lines associated with the BLR had measurable lags of order a couple of days when compared to the V band light curve (associated with the accretion disk). This result would agree with our ACFs, and would be a plausible explanation for the apparent 'dip' in our model ACFs when compared to our data ACFs. For us to confirm their results entirely, we would need better V band light curves as well as simultaneous emission line measurements. Kriss et al. [54] found an accretion disk alone was not enough to accurately model the reprocessing in *NGC 7469*. In summary, there is strong physical justification that with the addition of a BLR in our model, our model and data ACFs would have appeared much more similar at timescales of a few days. Using this, one could then obtain a reasonable estimate of the physical scale of the BLR via reverberation mapping [55, 56]. Interestingly, BLR size is believed to depend more strongly on the specific accretion rate rather than central black hole mass [57].

Although the BLR would lie further from the x-ray corona (and hence receive lower x-ray flux than the disk), the solid angle of the BLR when viewed from the corona would be much larger (an example graphical description can be found in [58]). This would mean that the total reprocessing would be similar in scale to that of the disk. There is also the potential for dusty torus reprocessing, although it is probable that by this

point, the x-ray flux is too small to produce a measurable contribution to lower energy light curves when measured from Earth given the combined effects of optical depth [59] and distance from the corona [58].

In this section we have presented a small selection of papers who all come to the same conclusion. The author was unable to find any recent papers which disagree with the BLR interpretation.[13] One could obtain a reasonable first-order estimate of the timescale of the BLR by adding a component similar in shape to the disk component, but with a larger initial delay and width, and then fitting the ACFs by varying response function parameters accordingly. The width of the best-fitting ACF corresponding to the BLR v could be initially guessed as $v = \sqrt{w^2 - u^2}$ where u is the width of the disk-only model ACF and w the width of the measured ACF.

---

[13]Whilst there is the possibility that there are some papers that reason BLR reprocessing is negligible, this is clearly not the widely-accepted view.

7 Project Extension – Inclined Accretion Disks

7.1 Theory of Response Function Calculation

As an extension to the project, we decided to look at modelling the inclined disk. Assuming a random distribution of disk inclinations, we would expect almost all accretion disks to have an inclination when viewed from Earth. This means that the axis passing through the centre of the black hole to the x-ray point source no longer directly points to us on Earth, but instead deviates by an angle i.[14] The resulting important change is the modification of the lag. This is because the rotational symmetry of the lag function is now removed, making the algebra of the system substantially more complicated. The accretion disk must now be described by the coordinates r and ϕ instead of just r:

$$\tau(r, \phi) = \frac{GM_\odot m}{c^2} \frac{\sqrt{h_X^2 + r^2} + h_X \cos i - r \cos \phi \sin i}{c}. \tag{51}$$

This result, taken from [19], defines $\phi = 0$ to be along the vector pointing on the accretion disk plane which has one directional component pointing towards Earth (plotted in two-dimensions as the white arrow in figure 11). We assume that the geometry of the AGN system itself does not change. Whilst this means that the x-ray radiation from the point source in the AGN system behaves the same, the observed response from Earth is modified. A plot of the lags projected onto a disk surface as viewed from Earth, equivalent to the polar function $r(\tau, \phi)$, is provided as figure 11. A derivation of the complicated equation $r(\tau, \phi)$ is performed in the appendix as section A.
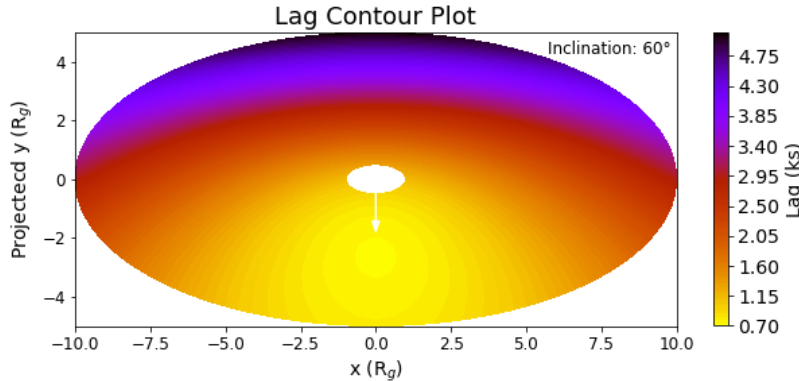

Figure 11: A contour plot of lags for $r < 10$ for a disk with $i = 60°$ and all other parameters the same as in figure 4. The y-axis is scaled to account for projection due to the inclination, making the disk appear broader than tall. The plot demonstrates how we expect the responses of inclined disks to be vastly more complicated as the shortest lag is no longer at the inner edge of the disk and the lags are no longer rotationally symmetric. A derivation of the equations of constant lag in polar form is provided in the appendix as section A.

We theorised a response function could be derived via the fundamental theorem of calculus and the multi-variable chain rule, a pair of techniques which we later independently tested on the face-on disk, deriving exactly the same response function as equation (40).[15] Utilising both these calculus techniques, we derived

---

[14]A common alternative notation uses the angle θ measured from the disk plane to the Earth-pointing vector. It is equivalent to $90° - i$.

[15]The derivation of this is similar to the one printed in the first two appendix sections except one starts with $i = 0$, meaning r only depends on τ, not ϕ. Our derivation in section 3.2.2 is arguably more intuitive so we do not reproduce the face-on disk derivation with the alternative method.

the following general response function for the inclined disk:

$$\frac{\partial(\Delta L)}{\partial \tau} = \frac{\partial(\Delta L)}{\partial r}\frac{\partial r}{\partial \tau}, \tag{52}$$

where

$$\frac{\partial(\Delta L)}{\partial r} = 2\pi \cos i \int_{\nu_{\min}}^{\nu_{\max}} [B_\nu(T_{\text{new}}(r) - B_\nu(T(r))] \, 2 \cdot 2\pi r \left(\frac{GM_\odot m}{c^2}\right)^2 \, d\nu, \tag{53}$$

and

$$\frac{\partial r}{\partial \tau} = \frac{-2c^3}{GM_\odot m}\left[\left\{\frac{-1 + \frac{\beta}{\sqrt{\beta^2 - 4\alpha\gamma}}}{2\alpha}\right\}\cos\phi\sin i - \frac{\varepsilon}{\sqrt{\beta^2 - 4\alpha\gamma}}\right]. \tag{54}$$

All terms not previously defined, along with the cumbersome derivation of the above three equations, are provided in the appendix in sections A and B. An important subtlety is the inclusion of a $\cos i$ term which reflects the reduction in flux of an off-angle disk when viewed from Earth.

An alternative method to ours was proposed by [38] and utilised again in [37].[16] This method involves calculating the effective areas of intersecting paraboloids formed by lags and disk emission. The derivation of this method is well beyond the scope of this project, although the end result is arguably simpler than the one we have produced above.

7.2   Theoretical Physical Implications

For small inclinations, the only noticeable effect measured on Earth is a reduction in the lag of the peak of the response function. This is because one side of the disk is slightly closer to Earth. To first order, $\cos i$, when $i \approx 0$, is equal to 1 so the flux change measured on Earth is negligible. As the inclination increases further, the response function begins to get sharper [19] but the flux begins to drop noticeably. For large inclinations, it is likely that the response function is wildly different due to obscuring of the disk by the dusty torus [58] or even parts of the galaxy. Given that the effects of small inclinations are negligible, our model used in this study was deemed suitable for a large proportion of galaxies, including *NGC 4593*. For galaxies with large inclinations, an updated model would have been required.

---

[16]It is quite long so we have not reproduced it here, but is explained in detail in both cited papers.

8 Future Work – Improving our Model

There are many improvements and additions one could make to our model. The most important would be the inclusion of the effects of a BLR which would act as an additional reprocessing component as discussed above in section 6.3. Another important improvement would be the inclusion of the effects of inclination as explained in section 7 and derived in the appendix. There are a few other, less important, effects that we could model in future. In our model, we have assumed the disk to be practically flat but have used non-flatness to explain the optical depth. It is generally believed that accretion disks flare and get thicker at larger radii [27]. This not only affects the optical depth that we already considered in our second, improved model, but also the solid angle of the disk when viewed from the x-ray corona. The larger solid angle has the effect of increasing the amount of x-ray flux absorbed by the disk and hence increasing the magnitude of the response function, especially at larger radii. Another property of the system affecting the solid angle and hence response function is the shape and size of the x-ray corona. Throughout the project, we assumed a point-source directly above the centre of the black hole, known as the lamppost model. Although definitely a simplification, it is a reasonable one [60] and it is likely modification of our model would affect results negligibly. A more realistic model is possibly an orbiting diffuse corona in the shape of a halo above the disk [61]. If one were to include this, they would need to calculate the emissivity profile of the corona and they would have to include the effects of general relativity [62]. Our model did not include relativistic effects[17] but they may have noticeable ramifications of light-bending of x-rays towards the inner disk and photon-reddening as the black body photons climb out of the black hole's potential well [19]. Another possible improvement is the consideration of a non-steady state accretion disk. The *SS Model* assumes that $\dot{m}$ is constant. Variations in the inflow of material can affect not only the material density and temperature, but optical depth as well and hence the amount of reprocessing. However, this would likely be the most complex of all the improvements suggested and would not be a priority. One final suggestion by the author is to more accurately model the albedo as suggested by [37]. A constant albedo approximation is probably safe for x-ray photons of a small range of energies but for larger ranges, the differences in disk reflectivity would become noticeable.

---

[17]Other than a disk inner edge.

9 Conclusions

In this project, we attempted to explain the observed UV/optical variability in AGN via disk reprocessing of x-ray radiation from a point source corona. We successfully established a unique semi-analytical formalism for calculating response functions without the need to normalise them. We found a simple thin-disk *SS Model* combined with x-ray absorption to be unsatisfactory, having to include the effects of optical depth $\propto \left(1 - \left(\frac{r_{\text{in}}}{r}\right)^{1/2}\right)^{4/5}$ due to disk thinning at small radii, to produce physical response functions. The model produced plausible theoretical temperature profiles and spectra, consistent with others found in the literature. We convolved our response functions with real x-ray light curves from Seyfert galaxy *NGC 4593* to produce model UV/optical light curves and compared them with real UV/optical light curves via auto-correlation functions. Our analysis showed our disk-only model was unable to explain the observed light curves as variability over timescales of 2-3 days required an extra component. We reasoned that the inclusion of a BLR could explain the difference in the timescales. This result is consistent with results of others in the literature. We then presented an introductory analysis of the inclined disk system and presented a possible semi-analytical algebraic solution with its corresponding derivation in the appendix. Finally, we presented a discussion of a range of ideas to improve the model to more accurately describe the AGN system via an analysis of different suggestions in the literature. These included a more accurate representation of the shape of the x-ray corona, thought to be shaped closer to a halo than a point source. Overall, although our model was not able to fully describe the observed UV/optical variability in AGN, it provided more evidence to the argument that UV/optical variability in AGN is powered by x-ray reprocessing by an accretion disk and a BLR.

References

[1] Gregory A. Shields. "A Brief History of Active Galactic Nuclei". In: *PASP* 111.760 (June 1999), pp. 661–678. ISSN: 1538-3873. DOI: 10.1086/316378. URL: http://dx.doi.org/10.1086/316378.

[2] E. E. Salpeter. "Accretion of Interstellar Matter by Massive Objects." In: *ApJ* 140 (Aug. 1964), pp. 796–800. DOI: 10.1086/147973.

[3] Ya. B. Zel'dovich. "The Fate of a Star and the Evolution of Gravitational Energy Upon Accretion". In: *Soviet Physics Doklady* 9 (Sept. 1964), p. 195.

[4] N. I. Shakura and R. A. Sunyaev. "Reprint of 1973A&A....24..337S. Black holes in binary systems. Observational appearance." In: *A&A* 500 (June 1973), pp. 33–51.

[5] Matias Montesinos. *Review: Accretion Disk Theory.* 2012. arXiv: 1203.6851 [astro-ph.HE].

[6] I. D. Novikov and K. S. Thorne. "Astrophysics of black holes." In: *Black Holes (Les Astres Occlus).* Jan. 1973, pp. 343–450.

[7] C. D. Impey. "Active Galactic Nuclei Across the Electromagnetic Spectrum". In: *Frontiers of Space And Ground-Based Astronomy: The Astrophysics of the 21st Century.* Ed. by W. Wamsteker, M. S. Longair, and Y. Kondo. Dordrecht: Springer Netherlands, 1994, pp. 685–686. ISBN: 978-94-011-0794-5. DOI: 10.1007/978-94-011-0794-5_111.

[8] Jong-Hak Woo and C. Megan Urry. "Active Galactic Nucleus Black Hole Masses and Bolometric Luminosities". In: *ApJ* 579.2 (Nov. 2002), pp. 530–544. DOI: 10.1086/342878. arXiv: astro-ph/0207249 [astro-ph].

[9] P. Uttley, I. M. McHardy, and I. E. Papadakis. "Measuring the broad-band power spectra of active galactic nuclei with RXTE". In: *MNRAS* 332.1 (May 2002), pp. 231–250. DOI: 10.1046/j.1365-8711.2002.05298.x. arXiv: astro-ph/0201134 [astro-ph].

[10] Roger Blandford, David Meier, and Anthony Readhead. "Relativistic Jets from Active Galactic Nuclei". In: *ARAA* 57 (Aug. 2019), pp. 467–509. DOI: 10.1146/annurev-astro-081817-051948. arXiv: 1812.06025 [astro-ph.HE].

[11] E. Bon and N. Gavrilović. "The Broad Line Region geometry: AGN with single peaked line profiles". In: *Memorie della Societa Astronomica Italiana Supplementi* 15 (Jan. 2010), p. 171.

[12] Rachel E. Mason. "Dust in the torus of the AGN unified model". In: *PlanSS* 116 (Oct. 2015), pp. 97–101. ISSN: 0032-0633. DOI: 10.1016/j.pss.2015.02.013. URL: http://dx.doi.org/10.1016/j.pss.2015.02.013.

[13] Y. Y. Zhou et al. "Statistical Properties of the Big Blue Bump in Active Galactic Nuclei". In: *ApJL* 475.1 (Jan. 1997), pp. L9–L12. DOI: 10.1086/310451.

[14] M. J. Page et al. "The Evolutionary Sequence of Active Galactic Nuclei and Galaxy Formation Revealed". In: *ApJL* 611.2 (Aug. 2004), pp. L85–L88. DOI: 10.1086/423892. arXiv: astro-ph/0407171 [astro-ph].

[15] P. Arévalo and P. Uttley. "Investigating a fluctuating-accretion model for the spectral-timing properties of accreting black hole systems". In: *MNRAS* 367.2 (Apr. 2006), pp. 801–814. DOI: 10.1111/j.1365-2966.2006.09989.x. arXiv: astro-ph/0512394 [astro-ph].

[16] F. Haardt and L. Maraschi. "A Two-Phase Model for the X-Ray Emission from Seyfert Galaxies". In: *ApJL* 380 (Oct. 1991), p. L51. DOI: 10.1086/186171.

[17] Ian Robson. "An Overview of AGN". In: *Activity in Galaxies and Related Phenomena*. Ed. by Y. Terzian, E. Khachikian, and D. Weedman. Vol. 194. Jan. 1999, p. 3.

[18] R. D. Blandford and C. F. McKee. "Reverberation mapping of the emission line regions of Seyfert galaxies and quasars." In: *ApJ* 255 (Apr. 1982), pp. 419–439. DOI: 10.1086/159843.

[19] Duncan Cameron. "The relationship between UV and Optical variability and X-ray variability in Active Galactic Nuclei, Thesis for the degree of Doctor of Philosophy, University of Southampton". In: (Feb. 2014).

[20] Edward M. Cackett, Keith Horne, and Hartmut Winkler. "Testing thermal reprocessing in active galactic nuclei accretion discs". In: *MNRAS* 380.2 (Sept. 2007), pp. 669–682. DOI: 10.1111/j.1365-2966.2007.12098.x. arXiv: 0706.1464 [astro-ph].

[21] I. M. McHardy et al. "X-ray/UV/optical variability of NGC 4593 with Swift: reprocessing of X-rays by an extended reprocessor". In: *MNRAS* 480.3 (Nov. 2018), pp. 2881–2897. DOI: 10.1093/mnras/sty1983. arXiv: 1712.04852 [astro-ph.HE].

[22] Misty C. Bentz et al. "The Low-luminosity End of the Radius-Luminosity Relationship for Active Galactic Nuclei". In: *ApJ* 767.2, 149 (Apr. 2013), p. 149. DOI: 10.1088/0004-637X/767/2/149. arXiv: 1303.1742 [astro-ph.CO].

[23] R. Maiolino and G. H. Rieke. "Low-Luminosity and Obscured Seyfert Nuclei in Nearby Galaxies". In: *ApJ* 454 (Nov. 1995), p. 95. DOI: 10.1086/176468.

[24] Kelly D. Denney et al. "The Mass of the Black Hole in the Seyfert 1 Galaxy NGC 4593 from Reverberation Mapping". In: *ApJ* 653.1 (Dec. 2006), pp. 152–158. DOI: 10.1086/508533. arXiv: astro-ph/0608406 [astro-ph].

[25] Carl K. Seyfert. "Nuclear Emission in Spiral Nebulae." In: *ApJ* 97 (Jan. 1943), p. 28. DOI: 10.1086/144488.

[26] Carl Friedrich Weizsäcker. "Die Rotation kosmischer Gasmassen". In: *Zeitschrift für Naturforschung A* 3.8-11 (1948), pp. 524–539. DOI: doi:10.1515/zna-1948-8-1118. URL: https://doi.org/10.1515/zna-1948-8-1118.

[27] Juhan Frank, Andrew R King, and Derek J Raine. *Accretion Power in Astrophysics*. 3rd ed. Cambridge Univ. Pr, 1985. ISBN: 9780521245302.

[28] Robert F. Penna et al. "The Shakura-Sunyaev viscosity prescription with variable $\alpha(r)$". In: *MNRAS* 428.3 (Nov. 2012), pp. 2255–2274. ISSN: 0035-8711. DOI: 10.1093/mnras/sts185. eprint: https://academic.oup.com/mnras/article-pdf/428/3/2255/3669563/sts185.pdf. URL: https://doi.org/10.1093/mnras/sts185.

[29] Jelle Kaastra. *Accretion Physics*. URL: https://personal.sron.nl/~kaastra/leiden2017/lnotes_part7.pdf (visited on 03/19/2021).

[30] M. C. Begelman and J. E. Pringle. "Accretion discs with strong toroidal magnetic fields". In: *MNRAS* 375.3 (Mar. 2007), pp. 1070–1076. DOI: 10.1111/j.1365-2966.2006.11372.x. arXiv: astro-ph/0612300 [astro-ph].

[31] Amir Jafari. *Magnetic Fields in Accretion Disks: A Review*. 2019. arXiv: 1904.09677 [astro-ph.HE].

[32] James M. Bardeen, William H. Press, and Saul A. Teukolsky. "Rotating Black Holes: Locally Non-rotating Frames, Energy Extraction, and Scalar Synchrotron Radiation". In: *ApJ* 178 (Dec. 1972), pp. 347–370. DOI: 10.1086/151796.

[33] C. J. Nixon et al. "Retrograde accretion and merging supermassive black holes". In: *MNRAS* 412.3 (Apr. 2011), pp. 1591–1598. DOI: 10.1111/j.1365-2966.2010.17952.x. arXiv: 1011.1914 [astro-ph.HE].

[34] Eugenie Samuel Reich. "Spin rate of black holes pinned down". In: *Nature* 500.7461 (Aug. 2013), p. 135. DOI: 10.1038/500135a.

[35] L. Ducci et al. "Exploring the role of X-ray reprocessing and irradiation in the anomalous bright optical outbursts of A0538-66". In: *A&A* 624, A9 (Apr. 2019), A9. DOI: 10.1051/0004-6361/201834390. arXiv: 1903.02918 [astro-ph.HE].

[36] Marek Gierliński, Chris Done, and Kim Page. "X-ray irradiation in XTE J1817-330 and the inner radius of the truncated disc in the hard state". In: *MNRAS* 388.2 (Aug. 2008), pp. 753–760. DOI: 10.1111/j.1365-2966.2008.13431.x. arXiv: 0803.0496 [astro-ph].

[37] Demosthenes Kazanas and Sergei Nayakshin. "Modeling the X-Ray-Optical Correlations in NGC 3516". In: *ApJ* 550.2 (Apr. 2001), pp. 655–667. DOI: 10.1086/319786. arXiv: astro-ph/0007421 [astro-ph].

[38] Andrew J. Berkley, Demosthenes Kazanas, and Jonathan Ozik. "Modeling the X-Ray–Ultraviolet Correlations in NGC 7469". In: *The Astrophysical Journal* 535.2 (June 2000), pp. 712–720. DOI: 10.1086/308880. URL: https://doi.org/10.1086/308880.

[39] E. Rokaki and C. Magnan. "Correlated variations of lines and continuum by disc reprocessing in NGC 5548." In: *A&A* 261 (July 1992), pp. 41–46.

[40] Kelly D. Denney et al. "The Mass of the Black Hole in the Seyfert 1 Galaxy NGC 4593 from Reverberation Mapping". In: *ApJ* 653.1 (Dec. 2006), pp. 152–158. DOI: 10.1086/508533. arXiv: astro-ph/0608406 [astro-ph].

[41] M. R. S. Hawkins. "Timescale of variation and the size of the accretion disc in active galactic nuclei". In: *A&A* 462.2 (Feb. 2007), pp. 581–589. DOI: 10.1051/0004-6361:20066283. arXiv: astro-ph/0611491 [astro-ph].

[42] David N. Burrows et al. "The Swift X-Ray Telescope". In: *SSR* 120.3-4 (Oct. 2005), pp. 165–195. DOI: 10.1007/s11214-005-5097-2. arXiv: astro-ph/0508071 [astro-ph].

[43] Peter W. A. Roming et al. "The Swift Ultra-Violet/Optical Telescope". In: *SSR* 120.3-4 (Oct. 2005), pp. 95–142. ISSN: 1572-9672. DOI: 10.1007/s11214-005-5095-4. URL: http://dx.doi.org/10.1007/s11214-005-5095-4.

[44] T. S. Poole et al. "Photometric calibration of the Swift ultraviolet/optical telescope". In: *MNRAS* 383.2 (Jan. 2008), pp. 627–645. DOI: 10.1111/j.1365-2966.2007.12563.x. arXiv: 0708.2259 [astro-ph].

[45] A. A. Breeveld et al. "An Updated Ultraviolet Calibration for the Swift/UVOT". In: *Gamma Ray Bursts 2010*. Ed. by J. E. McEnery, J. L. Racusin, and N. Gehrels. Vol. 1358. American Institute of Physics Conference Series. Aug. 2011, pp. 373–376. DOI: 10.1063/1.3621807. arXiv: 1102.4717 [astro-ph.IM].

[46] Michael Koss et al. "Host Galaxy Properties of the Swift Bat Ultra Hard X-Ray Selected Active Galactic Nucleus". In: *ApJ* 739.2, 57 (Oct. 2011), p. 57. DOI: 10.1088/0004-637X/739/2/57. arXiv: 1107.1237 [astro-ph.CO].

[47] Aidan C. Crook et al. "Groups of Galaxies in the Two Micron All Sky Redshift Survey". In: *ApJ* 655.2 (Feb. 2007), pp. 790–813. DOI: 10.1086/510201. arXiv: astro-ph/0610732 [astro-ph].

[48] R. A. Edelson and J. H. Krolik. "The Discrete Correlation Function: A New Method for Analyzing Unevenly Sampled Variability Data". In: *ApJ* 333 (Oct. 1988), p. 646. DOI: 10.1086/166773.

[49] S. Vaughan et al. "On characterizing the variability properties of X-ray light curves from active galaxies". In: *MNRAS* 345.4 (Nov. 2003), pp. 1271–1284. DOI: 10.1046/j.1365-2966.2003.07042.x. arXiv: astro-ph/0307420 [astro-ph].

[50] Kirk T. Korista and Michael R. Goad. "The Variable Diffuse Continuum Emission of Broad-Line Clouds". In: *ApJ* 553.2 (June 2001), pp. 695–708. DOI: 10.1086/320964. arXiv: astro-ph/0101117 [astro-ph].

[51] K. T. Korista and M. R. Goad. "Quantifying the impact of variable BLR diffuse continuum contributions on measured continuum interband delays". In: *MNRAS* 489.4 (Nov. 2019), pp. 5284–5300. DOI: 10.1093/mnras/stz2330. arXiv: 1908.07757 [astro-ph.GA].

[52] I. M. McHardy et al. "Swift monitoring of NGC 5548: X-ray reprocessing and short-term UV/optical variability". In: *MNRAS* 444.2 (Oct. 2014), pp. 1469–1474. DOI: 10.1093/mnras/stu1636. arXiv: 1407.6361 [astro-ph.HE].

[53] Aaron J. Barth et al. "The Lick AGN Monitoring Project 2011: Fe II Reverberation from the Outer Broad-line Region". In: *ApJ* 769.2, 128 (June 2013), p. 128. DOI: 10.1088/0004-637X/769/2/128. arXiv: 1304.4643 [astro-ph.CO].

[54] Gerard A. Kriss et al. "A High Signal-to-Noise Ultraviolet Spectrum of NGC 7469: New Support for Reprocessing of Continuum Radiation". In: *ApJ* 535.1 (May 2000), pp. 58–72. DOI: 10.1086/308840. arXiv: astro-ph/9912204 [astro-ph].

[55] A. Wandel, B. M. Peterson, and M. A. Malkan. "Central Masses and Broad-Line Region Sizes of Active Galactic Nuclei. I. Comparing the Photoionization and Reverberation Techniques". In: *The Astrophysical Journal* 526.2 (Dec. 1999), pp. 579–591. DOI: 10.1086/308017. URL: https://doi.org/10.1086/308017.

[56] Ying Zu, C. S. Kochanek, and Bradley M. Peterson. "An Alternative Approach to Measuring Reverberation Lags in Active Galactic Nuclei". In: *ApJ* 735.2, 80 (July 2011), p. 80. DOI: 10.1088/0004-637X/735/2/80. arXiv: 1008.0641 [astro-ph.CO].

[57] Xue-Guang Zhang, Deborah Dultzin-Hacyan, and Ting-Gui Wang. "The size of broad-line regions of low-luminosity active galactic nuclei". In: *MNRAS* 374.2 (Dec. 2006), pp. 691–696. ISSN: 0035-8711. DOI: 10.1111/j.1365-2966.2006.11182.x. eprint: https://academic.oup.com/mnras/article-pdf/374/2/691/4888689/mnras0374-0691.pdf. URL: https://doi.org/10.1111/j.1365-2966.2006.11182.x.

[58] Czerny, B. and Hryniewicz, K. "The origin of the broad line region in active galactic nuclei". In: *A&A* 525 (2011), p. L8. DOI: 10.1051/0004-6361/201016025. URL: https://doi.org/10.1051/0004-6361/201016025.

[59] Ari Laor. "Evidence for Line Broadening by Electron Scattering in the Broad-Line Region of NGC 4395". In: *The Astrophysical Journal* 643.1 (May 2006), pp. 112–119. DOI: 10.1086/502798. URL: https://doi.org/10.1086/502798.

[60] D. Emmanoulopoulos et al. "General relativistic modelling of the negative reverberation X-ray time delays in AGN". In: *MNRAS* 439.4 (Mar. 2014), pp. 3931–3950. ISSN: 0035-8711. DOI: 10.1093/mnras/stu249. eprint: https://academic.oup.com/mnras/article-pdf/439/4/3931/3993578/stu249.pdf. URL: https://doi.org/10.1093/mnras/stu249.

[61] D. R. Wilkins and A. C. Fabian. "Understanding X-ray reflection emissivity profiles in AGN: locating the X-ray source". In: *MNRAS* 424.2 (Aug. 2012), pp. 1284–1296. DOI: 10.1111/j.1365-2966.2012.21308.x. arXiv: 1205.3179 [astro-ph.HE].

[62] E. M. Cackett et al. "Modelling the broad Fe Kα reverberation in the AGN NGC 4151". In: *MNRAS* 438.4 (Jan. 2014), pp. 2980–2994. ISSN: 0035-8711. DOI: 10.1093/mnras/stt2424. eprint: https://academic.oup.com/mnras/article-pdf/438/4/2980/3834413/stt2424.pdf. URL: https://doi.org/10.1093/mnras/stt2424.

Appendices

A   Derivation of Polar Form for $r(\tau, \phi)$

This derivation is provided as a useful tool for anyone wishing to perform inclined disk analysis. Starting with:

$$\tau(r, \phi) = \frac{GM_\odot m}{c^2} \frac{\sqrt{h_X^2 + r^2} + h_X \cos i - r \cos \phi \sin i}{c}, \tag{A-1}$$

we divide through by $GM_\odot m/c^3$ and obtain:

$$\varrho = \frac{\tau c^3}{GM_\odot m} = \sqrt{h_X^2 + r^2} + h_X \cos i - r \cos \phi \sin i. \tag{A-2}$$

Moving across terms:

$$\varepsilon + r \cos \phi \sin i = \varrho - h_X \cos i + r \cos \phi \sin i = \sqrt{h_X^2 + r^2}. \tag{A-3}$$

Squaring both sides:

$$\varepsilon^2 + 2\varepsilon r \cos \phi \sin i + r^2 \left(\cos \phi \sin i\right)^2 = r^2 + h_X^2, \tag{A-4}$$

and moving it all to one side:

$$\left(1 - \cos^2 \phi \sin^2 i\right) r^2 + \left(-2\varepsilon \cos \phi \sin i\right) r + h_X^2 - \varepsilon^2 = 0. \tag{A-5}$$

For visual simplicity, we define this to be equal to:

$$\alpha r^2 + \beta r + \gamma = 0, \tag{A-6}$$

which we solve via the quadratic formula to give us our polar equation for r for constant lags:

$$r = \frac{-\beta + \sqrt{\beta^2 - 4\alpha\gamma}}{2\alpha}. \tag{A-7}$$

We can safely ignore the negative solution for r as r is defined to be positive. To utilise this equation, simply pick the inclination of choice and the lag one wishes to measure at and plot r as a function of ϕ. The behaviour of the plot is quite complicated to explain in words but easily understood graphically. The author created an interactive plot utilising the online plotting software DESMOS which can be accessed here. One simply varies i_{deg} and τ_{lag} once the black hole mass, corona height, and inner disk radius have all been established. The plot updates in real time.

B   Theoretical Inclined Disk Response Function Derivation

The method shown below is a unique derivation of the response function of the inclined disk. This method can be utilised to derive the response function for the non-inclined disk although in that case it is much simpler due to some tricks of single variable calculus (i.e. the left half of equation (39)). Using the multi-variable chain rule we can write:

$$\frac{\partial(\Delta L)}{\partial \tau} = \frac{\partial(\Delta L)}{\partial r}\frac{\partial r}{\partial \tau} + \frac{\partial(\Delta L)}{\partial \phi}\frac{\partial \phi}{\partial \tau}. \tag{B-1}$$

As $\frac{\partial(\Delta L)}{\partial \phi} = 0$, this is equal to:

$$\frac{\partial(\Delta L)}{\partial \tau} = \frac{\partial(\Delta L)}{\partial r}\frac{\partial r}{\partial \tau}. \tag{B-2}$$

$\frac{\partial(\Delta L)}{\partial r}$ is defined as:

$$\frac{\partial(\Delta L)}{\partial r} = 2\pi \cos i \int_{\nu_{\min}}^{\nu_{\max}} [B_\nu(T_{\mathrm{new}}(r)) - B_\nu(T(r))]\, 2 \cdot 2\pi r \left(\frac{GM_\odot m}{c^2}\right)^2 d\nu. \tag{B-3}$$

It should be obvious how one obtains this from the definition of the difference of the two spectra L_ν and the fundamental theorem of calculus. Recall the definition of r as in equation (A-7). We can use this to write a definition of $\frac{\partial r}{\partial \tau}$ as (again using the multi-variable chain rule):

$$\frac{\partial r}{\partial \tau} = \frac{\partial r}{\partial \alpha}\frac{\partial \alpha}{\partial \tau} + \frac{\partial r}{\partial \beta}\frac{\partial \beta}{\partial \tau} + \frac{\partial r}{\partial \gamma}\frac{\partial \gamma}{\partial \tau}, \tag{B-4}$$

which after further manipulation enables us to write:

$$\frac{\partial r}{\partial \tau} = \frac{\partial r}{\partial \beta}\frac{\partial \beta}{\partial \varepsilon}\frac{\partial \varepsilon}{\partial \varrho}\frac{\partial \varrho}{\partial \tau} + \frac{\partial r}{\partial \gamma}\frac{\partial \gamma}{\partial \varepsilon}\frac{\partial \varepsilon}{\partial \varrho}\frac{\partial \varrho}{\partial \tau}. \tag{B-5}$$

After appropriate substitution we obtain:

$$\frac{\partial r}{\partial \tau} = \frac{-2c^3}{GM_\odot m}\left[\frac{\partial r}{\partial \beta}\cos\phi\sin i + \varepsilon \frac{\partial r}{\partial \gamma}\right], \tag{B-6}$$

where

$$\frac{\partial r}{\partial \beta} = \frac{-1 + \frac{\beta}{\sqrt{\beta^2 - 4\alpha\gamma}}}{2\alpha}, \tag{B-7}$$

and

$$\frac{\partial r}{\partial \gamma} = \frac{-1}{\sqrt{\beta^2 - 4\alpha\gamma}}. \tag{B-8}$$

Finally, substituting the two derivatives:

$$\frac{\partial r}{\partial \tau} = \frac{-2c^3}{GM_\odot m}\left[\left\{\frac{-1 + \frac{\beta}{\sqrt{\beta^2 - 4\alpha\gamma}}}{2\alpha}\right\}\cos\phi\sin i - \frac{\varepsilon}{\sqrt{\beta^2 - 4\alpha\gamma}}\right]. \tag{B-9}$$

Substituting both $\frac{\partial r}{\partial \tau}$ and equation (B-3) into equation (B-2), one obtains our theoretical semi-analytical response function. It must be noted the above result has not been fully tested so users should proceed with caution. To utilise this appendix section, one should plot equation (B-2) as a function of $\tau(r, \phi)$, defined in

equation (A-1). One could do this by choosing a value of ϕ and varying r to calculate a 'virtual' response function of one angular coordinate. This then needs to be repeated for a large sample of ϕ values. One then needs to appropriately bin the 'virtual' response functions to merge them into an observable response function.

C Response Function Calculation Code

```python
1   import numpy as np
2   from scipy.integrate import simps as integrate
3   import pylab
4   from math import pi
5
6   #define constants
7   m_p = 1.6726231e-27
8   c = 2.99792458e8
9   sigma_SB = 5.67e-8
10  sigma_T = 6.652e-29
11  G = 6.67259e-11
12  M_sun = 1.99e30
13  h = 1.05457266e-34 * 2*pi #reduced planck constant times 2pi
14  k_B = 1.380658e-23
15  L_sun = 3.828e26
16
17  def T(r, m, mdot_E, a, h_x, L_x, A, x_ray = 0):
18      '''Calculates the temperature of the accretion disk at a radius r (in
19      gravitational units) given the black hole mass (in solar masses) and the
20      accretion rate (in eddington units), height of x ray source above disk
21      (in gravitational units), the xray luminosity (in watts) and the albedo.
22      The x-ray parameter is 1 for an illuminated disk, 0 otherwise.'''
23      eta = eddington_efficiency(a)
24      const = 3*m_p*c**5/(2*eta*sigma_T*sigma_SB*G*M_sun)
25      extra_r_factor = 1-(r_isco(a)/r)**(1/2)
26      T_old_forthpower = const * (mdot_E * extra_r_factor / (r**3*m))
27      const2 = c**4/(4*pi*sigma_SB*G**2*M_sun**2)
28      chi_0 = 1
29      optical_depth = (1-np.exp(-chi_0*(1-(r_isco(a)/r)**(1/2))**(4/5)))
30      xray_heating_term = x_ray * const2 * (1-A) * L_x * h_x * optical_depth / (m**2 *
        ↪  (h_x**2+r**2)**(3/2))
31      return (T_old_forthpower + xray_heating_term)**(1/4)
32
33  def B_nu(Ts, nus):
34      '''Calculates the blackbody function WHz^-1m^-2Sr^-1 and removes Nan values.
35      T and nu can both be inputted as arrays!'''
36      Ts_col = np.vstack(Ts)
37
38      B = 2*h*nus**3/c**2 / (np.exp(h * nus / (k_B * Ts_col)) - 1)
```

```python
39        return np.nan_to_num(B)

40

41   def r_isco(a):
42        '''Given the dimensionless spin parameter a from [-1, 1] calculates the
43        innermost stable circular orbit in gravitational radii. This function cleverly
44        uses special units to make equations simpler.'''
45        if abs(a) > 1:
46            raise Exception("a must lie on the closed interval [-1, 1]")
47        Z1 = 1 + (1-a**2)**(1/3)*((1+a)**(1/3)+(1-a)**(1/3))
48        Z2 = (3*a**2 + Z1**2)**(1/2)
49        Z3 = np.sign(a)*((3-Z1)*(3+Z1+2*Z2))**(1/2)
50        return 3 + Z2 - Z3

51

52   def eddington_efficiency(a):
53        '''Calculates the eddington efficiency dependent on the inner accretion disk
54        radius which is assumed to be at the ISCO. The ISCO depends on the dimensionless
55        spin parameter a.'''
56        return 1-(1-2/(3*r_isco(a)))**(1/2)

57

58   def D(r, m, h_x):
59        '''Calculates the extra distance light travels to a point on the disk and towards the
         ↪   observer'''
60        return G*M_sun*m/c**2 * (np.sqrt(r**2+h_x**2) + h_x)

61

62

63   def response(r, m, mdot_E, a, h_x, L_x, A, freqs):
64        '''Calculates the response function of our non-inclined disk.'''
65        T1 = T(r, m, mdot_E, a, h_x, L_x, A, x_ray = 0)
66        T2 = T(r, m, mdot_E, a, h_x, L_x, A, x_ray = 1)

67

68        '''Creates a 2x2 array of dimension (frequencies, radii)'''
69        B2 = B_nu(T2, freqs)
70        B1 = B_nu(T1, freqs)
71        deltaB = B2-B1

72

73        '''Integrates along the frequency axis to get Wm^-2Sr^-1 at each radius'''
74        deltaLs = integrate(deltaB, x = freqs, axis = 1)

75

76        '''Multiplies by all the other bits to get the correct final answer in Ws^-1!
         ↪   Hooray!'''
77        deltaLs *= 4*pi * G*M_sun*m/c * np.sqrt(r**2 + h_x**2) * 2*pi
```

```python
78      return deltaLs #our response function
79
80  '''Main block of codes starts here:'''
81  mass_BH = 5e7 # mass in solar unit
82  mdot_eddington = 0.05 #accrestion rate in eddington units
83  spin = 1 #dimensionless spin parameter
84  r_in = r_isco(spin)+1e-15 #gravitational units
85  r_out = 10**(3) #outer edge of disk
86  '''We have to add a small number to the innermost radius as other wise our T(r=r_isco)
    ↪   generates a 0 value
87  which causes our _inside_of_integral function to throw an error due to dividing by zero
    ↪   in the
88  exponential function inside of the blackbody function. This change of r_min has no
    ↪   noticable effect on results.'''
89
90  radii_data_points = 1000
91  radii = np.geomspace(r_in+1e-15, r_out, num = radii_data_points) #in gravitational units
92
93  l_X = 0.08 #x ray luminosity as fraction of L_Bol
94  L_X = l_X*1e12*L_sun #here we take the total xray emission as a fraction of L_Bol taken
    ↪   to be ~1e12 suns
95  h_X = 3 #+ radii[0] #x ray source height above disk in gravitational units
96  albedo = 0.3 #albedo
97
98  freq_data_points = 1000
99  freq_low =  1e5 #Hz
100 freq_high = 10**(17.5)
101 frequencies = np.geomspace(freq_low, freq_high, num = freq_data_points)
102
103 responses = response(radii, mass_BH, mdot_eddington, spin, h_X, L_X, albedo, frequencies)
104 taus = D(radii, mass_BH, h_X) / c
105
106 print("Total extra luminosity from disk response spin " + str(spin) + ":
    ↪   {:e}".format(integrate(responses, x = taus) / L_sun) + " L_")
107 pylab.figure(figsize = (10,8))
108 pylab.title("Response Functions", fontsize = 16)
109 pylab.plot(taus, responses, label = "Response")
110 pylab.xlabel("$\\tau$ (s)", fontsize = 14)
111 pylab.ylabel("$\\frac{\\partial[\\Delta L(r)]}{\\partial\\tau}$ (Ws$^{-1}$)", fontsize =
    ↪   14)
112 pylab.xscale("log")
```

```
113  #pylab.yscale("log")
114  pylab.xticks(fontsize = 12)
115  pylab.yticks(fontsize = 12)
116  pylab.legend(fontsize = 12)
117  #pylab.savefig("response.pdf", bbox_inches = 'tight')
118  pylab.show()
```
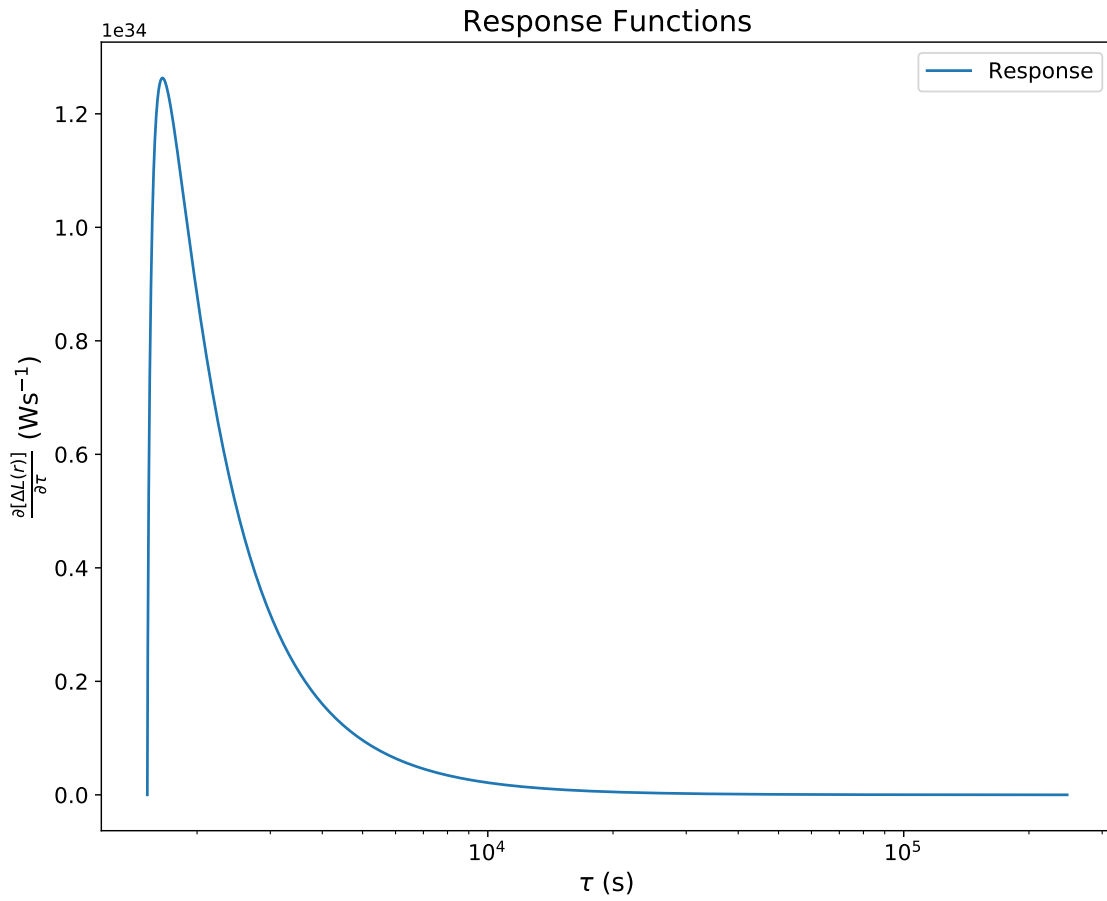

Figure 12: The plot generated by the above code. One simply stores 'responses' and 'taus' as data files for further manipulation.